Geophysical Journal International

Geophys. J. Int. (2015) **202,** 119–141 doi: 10.1093/gji/ggv133
GJI Marine geosciences and applied geophysics

Wave energy focusing to subsurface poroelastic formations to promote oil mobilization

Pranav M. Karve and Loukas F. Kallivokas

Department of Civil, Architectural and Environmental Engineering, The University of Texas at Austin, 30 *East Dean Keeton St., Stop* C1747, *Austin, TX* 78712, *USA. E-mail: loukas@mail.utexas.edu*

Accepted 2015 March 17. Received 2015 March 12; in original form 2014 August 24

SUMMARY

We discuss an inverse source formulation aimed at focusing wave energy produced by ground surface sources to target subsurface poroelastic formations. The intent of the focusing is to facilitate or enhance the mobility of oil entrapped within the target formation. The underlying forward wave propagation problem is cast in two spatial dimensions for a heterogeneous poroelastic target embedded within a heterogeneous elastic semi-infinite host. The semi-infiniteness of the elastic host is simulated by augmenting the (finite) computational domain with a buffer of perfectly matched layers. The inverse source algorithm is based on a systematic framework of partial-differential-equation-constrained optimization. It is demonstrated, via numerical experiments, that the algorithm is capable of converging to the spatial and temporal characteristics of surface loads that maximize energy delivery to the target formation. Consequently, the methodology is well-suited for designing field implementations that could meet a desired oil mobility threshold. Even though the methodology, and the results presented herein are in two dimensions, extensions to three dimensions are straightforward.

Key words: Numerical solutions; Inverse theory; Wave propagation.

1 INTRODUCTION

Efficient extraction of trapped particles from the pores of geological formations has important implications, among others, in enhanced oil recovery (EOR), purification of aquifers, transport of colloidal particles at waste disposal sites, etc. Traditionally, EOR has been the battleground for research and development of innovative methodologies for removal of crude oil particles from reservoirs. Propelled by the ever increasing oil demand and decrease in production from known reservoirs (IEO 2013), EOR methods aim at extraction of part of the original oil in place (OOIP), usually deemed irrecoverable by conventional recovery methods. Water or gas flooding, commonly used in conventional oil recovery, is unable to overcome the strong capillary forces governing fluid motion in the narrow pores, and leaves about 30–50 per cent of the OOIP behind (Lake 1989). EOR methods attempt removal of the trapped oil particles by injection of materials not normally present in reservoirs (solvents, polymers and steam). However, EOR processes involving infusion of chemicals suffer from low sweep efficiency problems in the low permeability areas, whereas thermal EOR (steam injection) faces challenges due to heat loss. Despite these challenges, EOR methods that use most of the infrastructure already in place at a (depleted) reservoir have been shown to be economically viable and effective (Lake 1989). Yet, significant reservoir capacity remains untapped, and alternative approaches maximizing recovery remain desirable.

Since seismic waves traveling through porous geological formations have been observed to stimulate fluid flow (Steinbrugge & Moran 1954; Smimova 1968; Voitov *et al.* 1972), it has been conjectured (Beresnev & Johnson 1994; Kostrov & Wooden 2002; Roberts & Abdel-Fattah 2009) that vibrations induced by wave sources placed on or below the ground surface can be used for EOR purposes instead of, or in addition to, the aforementioned methods. The wave-based, or seismic EOR methods, as they are commonly referred to, use various types of wave sources (e.g. Vibroseis trucks and/or wellbore hydraulic pumps) to illuminate the target formation. Since elastic waves suffer energy loss via radiation damping, intrinsic and apparent attenuation, a distant target formation may not receive the amount of wave energy required to effect the removal of trapped particles. Thus, a successful field implementation of a wave-based EOR method is contingent upon: (i) a reliable estimate of the magnitude of the motion threshold required for discharging the trapped particles, and (ii) the ability of (artificial) wave sources to generate sufficiently strong wave motion in the reservoir. These requirements necessitate pore-scale analysis of the fluid motion in narrow pores, when subjected to mechanical vibrations, as well as reservoir-scale wave motion studies.

The purpose of the pore-scale dynamics studies is twofold: they improve our understanding of the mechanisms responsible for the release of trapped particles, and they quantify the threshold motion needed for the removal of trapped particles. Kostrov & Wooden (2002)

© The Authors 2015. Published by Oxford University Press on behalf of The Royal Astronomical Society.

suggested two candidate mechanisms for vibration-based EOR: (i) dislodgement of oil droplets adhering to the pore wall into the flow of fluid, (ii) coalescence of two or more oil droplets into a bigger droplet having higher mobility. Roberts & Abdel-Fattah (2009) studied the release of *in situ* particles from Fontainebleau sandstone, induced by applying low frequency (26 Hz) stress stimulation in the laboratory. They reported enhanced particle release compared to that induced by flowing deionized water, and suggested three underlying mechanisms: (i) enhanced flushing or squeezing out of particles trapped in dead-end pores; (ii) forced particle detachment; and (iii) exposing of new detachment sites on the pore wall. Beresnev & Deng (2010) analysed the motion of a non-wetting fluid-blob in a sinusoidally varying 1-D channel under the assumption of two-phase core-annular Poiseuillean flow. They studied the relative motion between the channel wall and an oil droplet for various excitation frequencies to arrive at the threshold acceleration values, for which, the oil blob is squeezed through a narrow constriction in the channel. Deng & Cardenas (2013) improved the model suggested in Beresnev & Deng (2010) and reported values of threshold acceleration that conform more closely to computational fluid dynamics (CFD) simulations. Beresnev *et al.* (2011) conducted laboratory experiments to determine the threshold acceleration, and reported that the threshold value observed in experiments was about 3–4 times smaller than that predicted by CFD simulations. In Kurlenya & Serdyukov (1999), the authors reported significant and long-term changes in the properties and the composition of fluids in the oil producing strata due to partial degassing when subjected to a vibro-seismic field of low intensity (10^{-7}–$10^{-6}\,\mathrm{W\,m^{-2}}$). In Steinbrugge & Moran (1954), Smimova (1968) and Voitov *et al.* (1972), the authors have reported a sustained improvement in oil production after seismic events took place in the vicinity of the reservoirs. Beresnev & Johnson (1994) and Manga *et al.* (2012) have communicated details of many laboratory and field tests reporting enhancement of oil particle removal caused by subjecting test specimen, and even reservoirs, to mechanical vibrations. The pore-scale observations suggest that wave stimulation can be utilized for discharging trapped particles from pores of geological formations, provided the excitation is capable of delivering motion that exceeds the mobility threshold.

On the other hand, at reservoir scale, various sources of attenuation, as well as equipment limitations, impose restrictions on the magnitude of wave energy delivered to the target formation by wave motion actuators. Assessing the wave sources' ability to impart sufficiently strong motion requires reservoir-scale wave motion modeling. Jeong *et al.* (2011a) studied the wave motion induced by wellbore fluid-pressure oscillations in homogeneous and fractured reservoirs, and reported that wellbore action alone is not sufficient to cause exploitable oil mobility. However, they suggested that a fleet of surface sources (Vibroseis), with suitable spatiotemporal characteristics, may be able to produce sufficiently strong motion.

Thus, if the material properties of the reservoir and its surrounding formations are assumed known, the question becomes what should be the source frequency content and the source locations that maximize the wave motion in the target reservoir? To address the frequency content part of the question, in a rather simplistic manner, one could, conceivably, conduct a frequency sweep of monochromatic sources in search of an energy maximum at the target formation. However, conducting a combined sweep for both source locations and frequency content is, from a computational perspective, prohibitively expensive.

Alternatively, one could pose the problem as an inverse source problem, where the spatiotemporal source characteristics are sought, such that a predetermined motion metric in the target (e.g. kinetic energy) be maximized. The problem is akin to the inverse medium problem arising in exploration geophysics (Bamberger *et al.* 1979; Tarantola 1984; Bunks *et al.* 1995; Epanomeritakis *et al.* 2008; Kallivokas *et al.* 2013), where minimization of the misfit between experimentally collected and computationally obtained data is used to determine the properties of subterranean formations, subject to the underlying physics. Here too, the inverse source problem is similarly formulated as a constrained minimization problem, where minimization of the objective functional is tantamount to maximization of a motion metric in the target formation, and the governing physics are side-imposed as constraints. Jeong *et al.* (2011b) used the inverse source problem approach for optimizing the frequency content of surface sources, when the reservoir was modeled as an elastic inclusion. Since the motion of a trapped oil blob relative to the solid channel wall is used to define the extraction threshold in pore-scale studies (e.g. Deng & Cardenas 2013), in this article we extend previous work to account for a poroelastic target, while also simultaneously searching for both frequency content and optimal source location. To this end, we use Biot's equations of poroelastodynamics (Biot 1956) for the target and Navier's equations of motion for the elastic host. The elastic domain is truncated by perfectly matched layers (PMLs) to achieve a physically faithful simulation of the wave mechanics in the computational domain. We note that the development herein is cast in two spatial dimensions under plane strain assumptions. The formulation is, however, directly extensible to three dimensions. Field implementation aiming at either 2-D or 3-D conditions are feasible, and, based on the results reported herein, they are promising for enhancing mobility.

In the following, we describe the details of the formulation, the inverse source framework, the numerical implementation, and report numerical results that demonstrate the ability of the optimizer to suggest source locations and construct associated excitations, which can focus energy in the target formation.

2 THE FORWARD PROBLEM

2.1 Strong form

We consider the problem of wave propagation in a 2-D, heterogeneous, composite (elastic-poroelastic) halfspace. The forward problem consists of finding the displacement field in the domain of interest, given the boundary conditions and any applied excitations. We intend to use finite elements for the numerical solution of the forward problem. This choice, in turn, necessitates the truncation of the semi-infinite

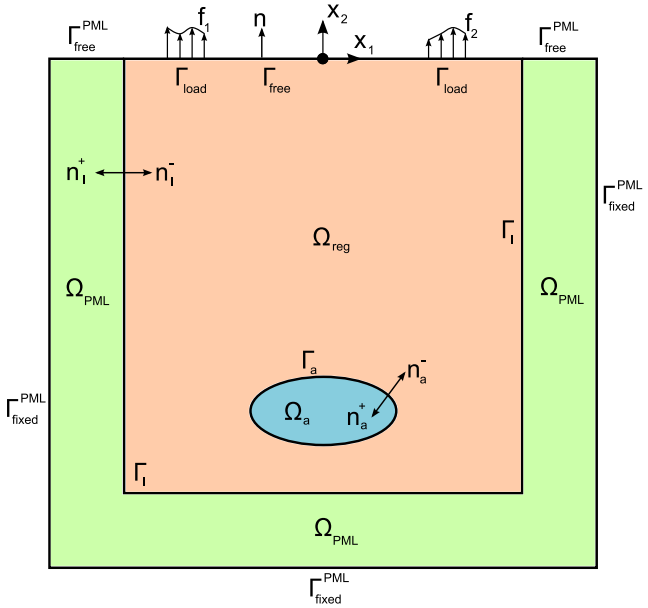

Figure 1. Problem definition.

domain: we use hybrid PMLs (Kucukcoban & Kallivokas 2013) to achieve a physically faithful simulation of wave propagation within the computational domain.

To fix ideas, consider the case of a porous rock (oil reservoir) represented by a poroelastic inclusion Ω_a, as shown in Fig. 1. The response in Ω_a is described, in general, by a solid and a fluid displacement field, $\mathbf{u}_a$, and $\mathbf{u}_f$, respectively. Herein, we favour the u–w formulation that uses the seepage displacement $\mathbf{w} = \phi(\mathbf{u}_f - \mathbf{u}_a)$, where ϕ is the porosity, to describe the fluid displacement field in Ω_a (Schanz 2009). A heterogeneous linear elastic solid occupying Ω_{reg}, surrounds the poroelastic target inclusion Ω_a. The response in Ω_{reg} is described by the $\mathbf{u}_b$ displacement field. Ω_{reg} is augmented by PMLs occupying Ω_{PML}. The governing equations in $\Omega = \Omega_a \cup \Omega_{reg} \cup \Omega_{PML}$, for time $t \in \mathbf{J} = (0, T]$, are given by:

$$\mathbf{div}\left[G_a\left(\nabla\mathbf{u}_a + \nabla\mathbf{u}_a^T\right) + \left\{\left(K_a - \frac{2}{3}G_a + \alpha^2\frac{R}{\phi^2}\right)\,\mathrm{div}\,\mathbf{u}_a + \alpha\frac{R}{\phi^2}\,\mathrm{div}\,\mathbf{w}\right\}\mathbf{I}\right] - \rho_a\ddot{\mathbf{u}}_a - \rho_f\ddot{\mathbf{w}} = \mathbf{0}, \quad \mathbf{x} \in \Omega_a, \tag{1a}$$

$$\mathbf{div}\left[\left\{\alpha\frac{R}{\phi^2}\,\mathrm{div}\,\mathbf{u}_a + \frac{R}{\phi^2}\,\mathrm{div}\,\mathbf{w}\right\}\mathbf{I}\right] - \rho_f\ddot{\mathbf{u}}_a - \rho_f\frac{1+C_1}{\phi}\ddot{\mathbf{w}} - \frac{1}{\kappa}\dot{\mathbf{w}} = \mathbf{0}, \quad \mathbf{x} \in \Omega_a, \tag{1b}$$

and,

$$\mathbf{div}\left[G_b\left(\nabla\mathbf{u}_b + \nabla\mathbf{u}_b^T\right) + \left\{\left(K_b - \frac{2}{3}G_b\right)\mathrm{div}\,\mathbf{u}_b\right\}\mathbf{I}\right] - \rho_b\ddot{\mathbf{u}}_b = \mathbf{0}, \quad \mathbf{x} \in \Omega_{reg}, \tag{2a}$$

$$\mathbf{div}\left(\dot{\mathbf{S}}^T\tilde{\Lambda}_e + \mathbf{S}^T\tilde{\Lambda}_p\right) - \rho_b\left(\mathbf{a}\ddot{\mathbf{u}}_b + \mathbf{b}\dot{\mathbf{u}}_b + \mathbf{c}\mathbf{u}_b\right) = \mathbf{0}, \quad \mathbf{x} \in \Omega_{PML}, \tag{2b}$$

$$\mathcal{D} : \left(\mathrm{a}\ddot{\mathbf{S}} + \mathrm{b}\dot{\mathbf{S}} + \mathrm{c}\dot{\mathbf{S}}\right) - \frac{1}{2}\left[\nabla\mathbf{u}_b\tilde{\Lambda}_p + \tilde{\Lambda}_p\left(\nabla\mathbf{u}_b\right)^T + \nabla\dot{\mathbf{u}}_b\tilde{\Lambda}_e + \tilde{\Lambda}_e\left(\nabla\dot{\mathbf{u}}_b\right)^T\right] = \mathbf{0}, \quad \mathbf{x} \in \Omega_{PML}, \tag{2c}$$

where an over-dot ($\dot{}$), denotes a derivative of the subtended entity with respect to time, and a colon (:), represents tensor inner product. In the above, and henceforth, we have suppressed the temporal and spatial dependencies for brevity. Eqs (1) are the poroelastodynamics equations derived by Biot (1956), expressed in the, so-called, u–w formulation (Schanz 2009). The definitions for symbols representing material constants in various parts of the computational domain are given in Table 1. In Ω_a, $\rho_a = (1-\phi)\rho_s + \phi\rho_f$ is the mass density of the composite; $\kappa = k/\mu$ denotes the fluid mobility, where k is the absolute permeability and μ is the fluid viscosity. The factor C_1 depends on the geometry of the pores: C_1 is related to the tortuosity of the fluid path, a_t, by the equation, $C_1 = 1 - a_t$ (Schanz 2009). Various approximations for C_1 can be found in the literature (Bourbié *et al.* 1987; Schanz 2009). Here, we use $C_1 = \frac{1}{2}(1 - \frac{1}{\phi})$. The boundary between the poroelastic and the elastic region is denoted by Γ_a. We assume that $\mathbf{w} \cdot \mathbf{n}_a^- = 0$ on Γ_a, that is, there is no fluid flow from the poroelastic inclusion into the elastic host. In Ω_a, the coupling between the solid and the fluid can be characterized by two parameters (Schanz 2009),

$$R = \frac{\phi^2 K_f K_s^2}{K_f\left(K_s - K_a\right) + \phi K_s\left(K_s - K_f\right)}, \quad Q = \frac{\phi\left((1-\phi)K_s - K_a\right)K_f K_s}{K_f\left(K_s - K_a\right) + \phi K_s\left(K_s - K_f\right)}. \tag{3}$$

Biot's effective stress coefficient, α, is given by,

$$\alpha = 1 - \frac{K_a}{K_s} = \phi\left(1 + \frac{Q}{R}\right). \tag{4}$$

Table 1. Symbols used for material properties in eqs (1) and (2).

Material property		Solid (grains)	Fluid	Saturated solid
Bulk modulus	Ω_{a}	K_s	K_f	K_{a}
	Ω_{reg}	K_{b}	–	–
	Ω_{PML}	K_{b}	–	–
Shear modulus	Ω_{a}	G_s	–	G_{a}
	Ω_{reg}	G_{b}	–	–
	Ω_{PML}	G_{b}	–	–
Mass density	Ω_{a}	ρ_s	ρ_f	ρ_{a}
	Ω_{reg}	ρ_{b}	–	–
	Ω_{PML}	ρ_{b}	–	–

Eqs (2) are the elastodynamics equations for an elastic medium augmented by PMLs (Kucukcoban & Kallivokas 2013). In particular, (2a) is the equilibrium equation, whereas (2b) is the combined constitutive law and kinematic condition equation. Eqs (2) introduce both displacement and stress unknowns in the PML, that is, they give rise to a mixed formulation, in favour of reducing the temporal complexity: as it can be shown, the resulting semi-discrete forms remain second-order in time. In eqs (2), $\mathbf{S}$ is the stress history tensor, given by,

$$\mathbf{S}(\mathbf{x},t)=\begin{bmatrix}\mathbf{S}_{11}(\mathbf{x},t) & \mathbf{S}_{12}(\mathbf{x},t)\\ \mathbf{S}_{21}(\mathbf{x},t) & \mathbf{S}_{22}(\mathbf{x},t)\end{bmatrix}=\int_0^t \boldsymbol{\sigma}(\mathbf{x},\tau)\,d\tau, \tag{5}$$

where, $\boldsymbol{\sigma}$ is the Cauchy stress tensor. $\tilde{\Lambda}_e$ and $\tilde{\Lambda}_p$ are components of the stretching tensor, and $\mathsf{a},\mathsf{b},\mathsf{c}$ are coefficients defining complex co-ordinate stretching in the PML region. Their detailed definitions are beyond the scope of this article and can be found in Kucukcoban & Kallivokas (2013). $\mathcal{D}$ is the compliance tensor, so that the constitutive relation can be expressed as $\mathcal{D}:\dot{\mathbf{S}}=\frac{1}{2}(\nabla\mathbf{u}_{\mathrm{b}}+\nabla\mathbf{u}_{\mathrm{b}}^T)$. For $t\in\mathsf{J}$, the governing equations are subjected to the following boundary conditions:

$$\mathbf{u}_{\mathrm{b}}=\mathbf{0},\qquad \mathbf{x}\in\Gamma_{\mathrm{fixed}}^{\mathrm{PML}}, \tag{6a}$$

$$\left[G_{\mathrm{b}}\left(\nabla\mathbf{u}_{\mathrm{b}}+\nabla\mathbf{u}_{\mathrm{b}}^T\right)+\left\{\left(K_{\mathrm{b}}-\frac{2}{3}G_{\mathrm{b}}\right)\ \mathrm{div}\ \mathbf{u}_{\mathrm{b}}\right\}\mathbf{I}\right]\mathbf{n}=\mathbf{f},\qquad \mathbf{x}\in\Gamma_{\mathrm{load}}, \tag{6b}$$

$$\left[G_{\mathrm{b}}\left(\nabla\mathbf{u}_{\mathrm{b}}+\nabla\mathbf{u}_{\mathrm{b}}^T\right)+\left\{\left(K_{\mathrm{b}}-\frac{2}{3}G_{\mathrm{b}}\right)\ \mathrm{div}\ \mathbf{u}_{\mathrm{b}}\right\}\mathbf{I}\right]\mathbf{n}=\mathbf{0},\qquad \mathbf{x}\in\Gamma_{\mathrm{free}}, \tag{6c}$$

$$\left(\dot{\mathbf{S}}^T\tilde{\Lambda}_e+\mathbf{S}^T\tilde{\Lambda}_p\right)\mathbf{n}=\mathbf{0},\qquad \mathbf{x}\in\Gamma_{\mathrm{free}}^{\mathrm{PML}}, \tag{6d}$$

interface conditions:

$$\mathbf{u}_{\mathrm{b}}^{+}=\mathbf{u}_{\mathrm{b}}^{-},\qquad \mathbf{x}\in\Gamma_{\mathrm{I}}, \tag{7a}$$

$$\left[G_{\mathrm{b}}\left(\nabla\mathbf{u}_{\mathrm{b}}+\nabla\mathbf{u}_{\mathrm{b}}^T\right)+\left\{\left(K_{\mathrm{b}}-\frac{2}{3}G_{\mathrm{b}}\right)\mathrm{div}\ \mathbf{u}_{\mathrm{b}}\right\}\mathbf{I}\right]\mathbf{n}_{\mathrm{I}}^{+}=-\left(\dot{\mathbf{S}}^T\tilde{\Lambda}_e+\mathbf{S}^T\tilde{\Lambda}_p\right)\mathbf{n}_{\mathrm{I}}^{-},\qquad \mathbf{x}\in\Gamma_{\mathrm{I}}; \tag{7b}$$

$$\mathbf{w}\cdot\mathbf{n}_{\mathrm{a}}^{-}=0,\qquad \mathbf{x}\in\Gamma_{\mathrm{a}}, \tag{7c}$$

$$\mathbf{u}_{\mathrm{a}}=\mathbf{u}_{\mathrm{b}},\qquad \mathbf{x}\in\Gamma_{\mathrm{a}}, \tag{7d}$$

$$\boldsymbol{\sigma}_{\mathrm{a}}^T\mathbf{n}_{\mathrm{a}}^{-}=-\boldsymbol{\sigma}_{\mathrm{b}}^T\mathbf{n}_{\mathrm{a}}^{+},\qquad \mathbf{x}\in\Gamma_{\mathrm{a}}; \tag{7e}$$

where,

$$\boldsymbol{\sigma}_{\mathrm{a}}=G_{\mathrm{a}}\left(\nabla\mathbf{u}_{\mathrm{a}}+\nabla\mathbf{u}_{\mathrm{a}}^T\right)+\frac{\alpha R}{\phi^2}(\mathrm{div}\ \mathbf{w})\,\mathbf{I}+\left[K_{\mathrm{a}}-\frac{2G_{\mathrm{a}}}{3}+\frac{\alpha^2 R}{\phi^2}\right](\mathrm{div}\ \mathbf{u}_{\mathrm{a}})\,\mathbf{I}, \tag{7f}$$

$$\boldsymbol{\sigma}_{\mathrm{b}}=G_{\mathrm{b}}\left(\nabla\mathbf{u}_{\mathrm{b}}+\nabla\mathbf{u}_{\mathrm{b}}^T\right)+\left[\left(K_{\mathrm{b}}-\frac{2}{3}G_{\mathrm{b}}\right)\ \mathrm{div}\ \mathbf{u}_{\mathrm{b}}\right]\mathbf{I}; \tag{7g}$$

and initial value conditions:

$$\mathbf{u}_{\mathrm{a}}(\mathbf{x},0)=\mathbf{0},\qquad \dot{\mathbf{u}}_{\mathrm{a}}(\mathbf{x},0)=\mathbf{0},\qquad \mathbf{x}\in\Omega_{\mathrm{a}}, \tag{8a}$$

$$\mathbf{u}_{\mathrm{b}}(\mathbf{x},0)=\mathbf{0},\qquad \dot{\mathbf{u}}_{\mathrm{b}}(\mathbf{x},0)=\mathbf{0},\qquad \mathbf{x}\in\Omega_{\mathrm{reg}}\cup\Omega_{\mathrm{PML}}, \tag{8b}$$

$$\mathbf{w}(\mathbf{x},0)=\mathbf{0},\qquad \dot{\mathbf{w}}(\mathbf{x},0)=\mathbf{0},\qquad \mathbf{x}\in\Omega_{\mathrm{a}}, \tag{8c}$$

$$\mathbf{S}(\mathbf{x},0)=\mathbf{0},\qquad \dot{\mathbf{S}}(\mathbf{x},0)=\mathbf{0},\qquad \mathbf{x}\in\Omega_{\mathrm{PML}}. \tag{8d}$$

The *strong form* of the forward problem can be stated as: given loads $\mathbf{f}(\mathbf{x}, t)$, find $\mathbf{w} \in \mathbf{H}^1_w(\Omega_\mathrm{a}) \times \mathsf{J}$, $\mathbf{u}_\mathrm{a} \in \mathbf{H}^1_u(\Omega_\mathrm{a}) \times \mathsf{J}$, $\mathbf{u}_\mathrm{b} \in \mathbf{H}^1_u(\Omega_\mathrm{reg} \cup \Omega_\mathrm{PML}) \times \mathsf{J}$ and $\mathbf{S} \in \mathcal{L}^2(\Omega_\mathrm{PML}) \times \mathsf{J}$, so that eqs (1) and (2) and boundary conditions (6)–(8) be satisfied, where, the pertinent function spaces for a scalar f, a vector $\mathbf{u}$ and a tensor $\mathbf{T}$ are given by:

$$L^2(\Omega) = \left\{ f : \int_\Omega |f|^2 d\Omega < \infty \right\}, \tag{9a}$$

$$\mathbf{L}^2(\Omega) = \left\{ \mathbf{u} : \mathbf{u} \in \left(L^2(\Omega)\right)^2 \right\}, \tag{9b}$$

$$\mathcal{L}^2(\Omega) = \left\{ \mathbf{T} : \mathbf{T} \in \left(L^2(\Omega)\right)^{2\times 2} \right\}, \tag{9c}$$

$$H^1_p(\Omega) = \left\{ f : \int_\Omega \left(|f|^2 + |\nabla f|^2\right) d\Omega < \infty \right\}, \tag{9d}$$

$$\mathbf{H}^1_u(\Omega) = \left\{ \mathbf{u} : \mathbf{u} \in \left(H^1_p(\Omega)\right)^2, \mathbf{u} = \mathbf{0} \text{ if } \mathbf{x} \in \Gamma^{\mathrm{PML}}_{\mathrm{fixed}} \right\}, \tag{9e}$$

$$\mathbf{H}^1_w(\Omega) = \left\{ \mathbf{u} : \mathbf{u} \in \left(H^1_p(\Omega)\right)^2, \mathbf{u} \cdot \mathbf{n}^-_\mathrm{a} = 0 \text{ if } \mathbf{x} \in \Gamma_\mathrm{a} \right\}. \tag{9f}$$

Next, we formulate the problem's weak form.

2.2 Weak form

We follow a conventional Galerkin approach: for example, we multiply eq. (1a) by a vector test function $\mathbf{v}_\mathrm{a}$, and eqs (2a) and (2b) by a vector test function $\mathbf{v}_\mathrm{b}$, integrate by parts on their corresponding domains, and add the resulting equations. Eq. (1b) is multiplied by a vector test function $\mathbf{q}$ and integrated over Ω_a. Furthermore, we multiply eq. (2c) by a tensor test function $\mathbf{T}$, and integrate over Ω_PML. After some simplifications, using the boundary conditions (6) and interface conditions (7), we arrive at the following weak form:

$$\begin{aligned}
&\int_{\Omega_\mathrm{a}} \left\{ \nabla \mathbf{v}_\mathrm{a} : \left[G_\mathrm{a} \left(\nabla \mathbf{u}_\mathrm{a} + \nabla \mathbf{u}_\mathrm{a}^T \right) + \alpha \frac{R}{\phi^2} \left(\operatorname{div} \mathbf{w}\right) \mathbf{I} + \left(K_\mathrm{a} - \frac{2G_\mathrm{a}}{3} + \frac{\alpha^2 R}{\phi^2} \right) \left(\operatorname{div} \mathbf{u}_\mathrm{a}\right) \mathbf{I} \right] + \mathbf{v}_\mathrm{a} \cdot \left(\rho_\mathrm{a} \ddot{\mathbf{u}}_\mathrm{a}\right) + \mathbf{v}_\mathrm{a} \cdot \left(\rho_f \ddot{\mathbf{w}}\right) \right\} d\Omega \\
&\quad + \int_{\Omega_\mathrm{reg}} \left\{ \nabla \mathbf{v}_\mathrm{b} : \left[G_\mathrm{b} \left(\nabla \mathbf{u}_\mathrm{b} + \nabla \mathbf{u}_\mathrm{b}^T \right) + \left(K_s - \frac{2G_\mathrm{b}}{3} \right) \left(\operatorname{div} \mathbf{u}_\mathrm{b}\right) \mathbf{I} \right] + \mathbf{v}_\mathrm{b} \cdot \rho_\mathrm{b} \ddot{\mathbf{u}}_\mathrm{b} \right\} d\Omega \\
&\quad + \int_{\Omega_\mathrm{PML}} \left\{ \nabla \mathbf{v}_\mathrm{b} : \left(\dot{\mathbf{S}}^T \tilde{\Lambda}_e + \mathbf{S}^T \tilde{\Lambda}_p \right) + \mathbf{v}_\mathrm{b} \cdot \rho_\mathrm{b} \left(\mathsf{a} \ddot{\mathbf{u}}_\mathrm{b} + \mathsf{b} \dot{\mathbf{u}}_\mathrm{b} + \mathsf{c} \mathbf{u}_\mathrm{b} \right) \right\} d\Omega = \int_{\Gamma_\mathrm{load}} \mathbf{v}_\mathrm{b} \cdot \mathbf{f} \, d\Gamma,
\end{aligned} \tag{10a}$$

$$\int_{\Omega_\mathrm{a}} \left\{ -\nabla \mathbf{q} : \left[\alpha \frac{R}{\phi^2} \left(\operatorname{div} \mathbf{u}_\mathrm{a}\right) \mathbf{I} + \frac{R}{\phi^2} \left(\operatorname{div} \mathbf{w}\right) \mathbf{I} \right] - \mathbf{q} \cdot \left[\rho_f \ddot{\mathbf{u}}_\mathrm{a} + \rho_f \frac{1 + C_1}{\phi} \ddot{\mathbf{w}} + \frac{1}{\kappa} \dot{\mathbf{w}} \right] \right\} d\Omega = 0, \tag{10b}$$

$$\int_{\Omega_\mathrm{PML}} \mathbf{T} : \left\{ \mathcal{D} : \left(\mathsf{a} \ddot{\mathbf{S}} + \mathsf{b} \dot{\mathbf{S}} + \mathsf{c} \dot{\mathbf{S}} \right) - \frac{1}{2} \left[\nabla \mathbf{u}_\mathrm{b} \tilde{\Lambda}_p + \tilde{\Lambda}_p \left(\nabla \mathbf{u}_\mathrm{b}\right)^T + \nabla \dot{\mathbf{u}}_\mathrm{b} \tilde{\Lambda}_e + \tilde{\Lambda}_e \left(\nabla \dot{\mathbf{u}}_\mathrm{b}\right)^T \right] \right\} d\Omega = 0. \tag{10c}$$

2.3 Semi-discrete form

Numerical solution of the forward problem requires spatiotemporal discretization. We introduce spatial discretization via shape functions $\Phi_w(\mathbf{x}) \in \mathbf{H}^1_{wh}(\Omega_\mathrm{a})$, $\Phi_u(\mathbf{x}) \in \mathbf{H}^1_{uh}(\Omega)$, and $\Psi(\mathbf{x}) \in \mathcal{L}^2_h(\Omega_\mathrm{PML})$. Thus, the trial and test functions are given by,

$$\mathbf{q} = \begin{bmatrix} \mathbf{q}_1^T \Phi_w(\mathbf{x}) \\ \mathbf{q}_2^T \Phi_w(\mathbf{x}) \end{bmatrix}, \quad \mathbf{w} = \begin{bmatrix} \mathbf{w}_1^T \Phi_w(\mathbf{x}) \\ \mathbf{w}_2^T \Phi_w(\mathbf{x}) \end{bmatrix},$$

$$\mathbf{v}_\mathrm{a} = \begin{bmatrix} \mathbf{v}_{\mathrm{a}_1}^T \Phi_u(\mathbf{x}) \\ \mathbf{v}_{\mathrm{a}_2}^T \Phi_u(\mathbf{x}) \end{bmatrix}, \quad \mathbf{u}_\mathrm{a} = \begin{bmatrix} \Phi_u(\mathbf{x})^T \mathbf{u}_{\mathrm{a}_1}(t) \\ \Phi_u(\mathbf{x})^T \mathbf{u}_{\mathrm{a}_2}(t) \end{bmatrix},$$

$$\mathbf{v}_\mathrm{b} = \begin{bmatrix} \mathbf{v}_{\mathrm{b}_1}^T \Phi_u(\mathbf{x}) \\ \mathbf{v}_{\mathrm{b}_2}^T \Phi_u(\mathbf{x}) \end{bmatrix}, \quad \mathbf{u}_\mathrm{b} = \begin{bmatrix} \Phi_u(\mathbf{x})^T \mathbf{u}_{\mathrm{b}_1}(t) \\ \Phi_u(\mathbf{x})^T \mathbf{u}_{\mathrm{b}_2}(t) \end{bmatrix},$$

$$\mathbf{T} = \begin{bmatrix} \mathbf{T}_{11}^T \Psi(\mathbf{x}) & \mathbf{T}_{12}^T \Psi(\mathbf{x}) \\ \mathbf{T}_{21}^T \Psi(\mathbf{x}) & \mathbf{T}_{22}^T \Psi(\mathbf{x}) \end{bmatrix}, \quad \mathbf{S} = \begin{bmatrix} \Psi(\mathbf{x})^T \mathbf{S}_{11}(t) & \Psi(\mathbf{x})^T \mathbf{S}_{12}(t) \\ \Psi(\mathbf{x})^T \mathbf{S}_{21}(t) & \Psi(\mathbf{x})^T \mathbf{S}_{22}(t) \end{bmatrix}. \tag{11}$$

Introducing approximants (11) into eqs (10a)–(10c) yields the following semi-discrete equation:

$$\mathbf{M}\ddot{\mathbf{d}} + \mathbf{C}\dot{\mathbf{d}} + \mathbf{K}\mathbf{d} = \mathbf{F}, \tag{12}$$

where,

$$\mathbf{d} = [\mathbf{w}_1 \mathbf{w}_2 \mathbf{u}_{a_1} \mathbf{u}_{a_2} \,|\, \mathbf{u}_{b_1}^{\text{reg}} \mathbf{u}_{b_2}^{\text{reg}} \,|\, \mathbf{u}_{b_1}^{\text{PML}} \mathbf{u}_{b_2}^{\text{PML}} \mathbf{S}_{11} \mathbf{S}_{22} \mathbf{S}_{12}]^T, \tag{13}$$

$$\mathbf{F} = [\mathbf{0}\ \mathbf{0}\ \mathbf{0}\ \mathbf{0} \,|\, \mathbf{F}^1\ \mathbf{F}^2 \,|\, \mathbf{0}\ \mathbf{0}\ \mathbf{0}\ \mathbf{0}\ \mathbf{0}]^T. \tag{14}$$

We note that **M**, **C** and **K** are, the global mass, damping and stiffness matrices, respectively, **d** is the vector of unknown displacements and stress histories, the latter only within the PML, and **F** is the force vector. The definitions of the element matrices that form the global matrices in eq. (12) are given in Appendix A.

The temporal dimension is now discretized using a time step Δt. We define the vector $\mathbf{d}_i \equiv \mathbf{d}(i\,\Delta t)$. Then, the spatiotemporally discretized system at time $t = (i+1)\Delta t$, can be written as,

$$\mathbf{M}\ddot{\mathbf{d}}_{i+1} + \mathbf{C}\dot{\mathbf{d}}_{i+1} + \mathbf{K}\mathbf{d}_{i+1} = \mathbf{F}_{i+1}. \tag{15}$$

We use Newmark's time integration scheme to integrate eq. (15) in time. At time $t = 0$:

$$\mathbf{M}\ddot{\mathbf{d}}_0 = \mathbf{F}_0 - \mathbf{C}\dot{\mathbf{d}}_0 - \mathbf{K}\mathbf{d}_0, \tag{16}$$

where, $\mathbf{d}_0$ and $\dot{\mathbf{d}}_0$ are the prescribed displacement and velocity vectors. For any time $t \in \mathsf{J}$, that is, for $i \geq 0$, we calculate the acceleration $\ddot{\mathbf{d}}_{i+1}$ by solving,

$$\mathbf{M}_{\text{eff}}\ddot{\mathbf{d}}_{i+1} = \mathbf{R}_{\text{eff}}, \tag{17}$$

where

$$\begin{aligned} \mathbf{M}_{\text{eff}} &= \mathbf{M} + \mathbf{C}\gamma(\Delta t) + \mathbf{K}(\Delta t)^2\beta \\ &= \mathbf{M} + b_4\mathbf{C} + b_2\mathbf{K}, \end{aligned} \tag{18}$$

$$\begin{aligned} \mathbf{R}_{\text{eff}} &= \mathbf{F}_{i+1} - \mathbf{K}\mathbf{d}_i - [\mathbf{C} + (\Delta t)\mathbf{K}]\,\dot{\mathbf{d}}_i - \left[(1-\gamma)(\Delta t)\mathbf{C} + \left(\frac{1}{2} - \beta\right)(\Delta t)^2\mathbf{K}\right]\ddot{\mathbf{d}}_i \\ &= \mathbf{F}_{i+1} - \mathbf{L}_0\mathbf{d}_i - \mathbf{L}_1\dot{\mathbf{d}}_i - \mathbf{L}_2\ddot{\mathbf{d}}_i. \end{aligned} \tag{19}$$

We, then, calculate the displacement and velocity at the $(i+1)$th time step using,

$$\begin{aligned} \mathbf{d}_{i+1} &= \mathbf{d}_i + (\Delta t)\dot{\mathbf{d}}_i + \left(\frac{1}{2} - \beta\right)(\Delta t)^2\ddot{\mathbf{d}}_i + \beta(\Delta t)^2\ddot{\mathbf{d}}_{i+1} \\ &= \mathbf{d}_i + b_0\dot{\mathbf{d}}_i + b_1\ddot{\mathbf{d}}_i + b_2\ddot{\mathbf{d}}_{i+1}, \end{aligned} \tag{20}$$

$$\begin{aligned} \dot{\mathbf{d}}_{i+1} &= \dot{\mathbf{d}}_i + (1-\gamma)(\Delta t)\ddot{\mathbf{d}}_i + \gamma(\Delta t)\ddot{\mathbf{d}}_{i+1} \\ &= \dot{\mathbf{d}}_i + b_3\ddot{\mathbf{d}}_i + b_4\ddot{\mathbf{d}}_{i+1}. \end{aligned} \tag{21}$$

The solution of the forward problem can be obtained by starting with $i = 0$ and marching in time ($i \leftarrow i+1$), using eqs (16)–(21). In eqs (17)–(21) we have introduced constants $b_0 \ldots b_4$ and matrices $\mathbf{L}_0, \mathbf{L}_1, \mathbf{L}_2$, for brevity. Their definitions are given below:

$$b_0 = \Delta t, \quad b_1 = \left(\tfrac{1}{2} - \beta\right)(\Delta t)^2, \quad b_2 = \beta(\Delta t)^2, \tag{22a}$$

$$b_3 = (1-\gamma)(\Delta t), \quad b_4 = \gamma(\Delta t), \tag{22b}$$

$$\mathbf{L}_0 = \mathbf{K}, \quad \mathbf{L}_1 = \mathbf{C} + b_0\mathbf{K}, \quad \mathbf{L}_2 = b_3\mathbf{C} + b_1\mathbf{K}. \tag{22c}$$

The step-by-step procedure given by eqs (16)–(21) can be represented as a solution of a linear system of equations (Kallivokas *et al.* 2013) given by,

$$\boldsymbol{Q}\boldsymbol{u} = \boldsymbol{f}, \tag{23}$$

where,

$$\boldsymbol{u} = [\ddot{\mathbf{d}}_0\ \dot{\mathbf{d}}_0\ \mathbf{d}_0\ \ddot{\mathbf{d}}_1\ \dot{\mathbf{d}}_1\ \mathbf{d}_1\ \cdots\ \ddot{\mathbf{d}}_N\ \dot{\mathbf{d}}_N\ \mathbf{d}_N\ ]^T, \tag{24}$$

$$\boldsymbol{f} = [\mathbf{F}_0\ \dot{\mathbf{d}}_0\ \mathbf{d}_0\ \mathbf{F}_1\ \mathbf{0}\ \mathbf{0}\ \cdots\ \mathbf{F}_N\ \mathbf{0}\ \mathbf{0}]^T, \tag{25}$$

$$Q = \left[\begin{array}{cccccccccccc}
\mathbf{M} & \mathbf{C} & \mathbf{K} & \mathbf{0} & \mathbf{0} & \mathbf{0} & \cdots & \mathbf{0} & \mathbf{0} & \mathbf{0} & \mathbf{0} & \mathbf{0} & \mathbf{0} \\
\mathbf{0} & \mathbf{I} & \mathbf{0} & \mathbf{0} & \mathbf{0} & \mathbf{0} & \cdots & \mathbf{0} & \mathbf{0} & \mathbf{0} & \mathbf{0} & \mathbf{0} & \mathbf{0} \\
\mathbf{0} & \mathbf{0} & \mathbf{I} & \mathbf{0} & \mathbf{0} & \mathbf{0} & \cdots & \mathbf{0} & \mathbf{0} & \mathbf{0} & \mathbf{0} & \mathbf{0} & \mathbf{0} \\
\hline
\mathbf{L}_2 & \mathbf{L}_1 & \mathbf{L}_0 & \mathbf{M}_{\text{eff}} & \mathbf{0} & \mathbf{0} & \cdots & \mathbf{0} & \mathbf{0} & \mathbf{0} & \mathbf{0} & \mathbf{0} & \mathbf{0} \\
-b_3\mathbf{I} & -\mathbf{I} & \mathbf{0} & -b_4\mathbf{I} & \mathbf{I} & \mathbf{0} & \cdots & \mathbf{0} & \mathbf{0} & \mathbf{0} & \mathbf{0} & \mathbf{0} & \mathbf{0} \\
-b_1\mathbf{I} & -b_0\mathbf{I} & -\mathbf{I} & -b_2\mathbf{I} & \mathbf{0} & \mathbf{I} & \cdots & \mathbf{0} & \mathbf{0} & \mathbf{0} & \mathbf{0} & \mathbf{0} & \mathbf{0} \\
\hline
\vdots & \vdots & \vdots & \vdots & \vdots & \vdots & \ddots & \vdots & \vdots & \vdots & \vdots & \vdots & \vdots \\
\hline
\mathbf{0} & \mathbf{0} & \mathbf{0} & \mathbf{0} & \mathbf{0} & \mathbf{0} & \cdots & \mathbf{L}_2 & \mathbf{L}_1 & \mathbf{L}_0 & \mathbf{M}_{\text{eff}} & \mathbf{0} & \mathbf{0} \\
\mathbf{0} & \mathbf{0} & \mathbf{0} & \mathbf{0} & \mathbf{0} & \mathbf{0} & \cdots & -b_3\mathbf{I} & -\mathbf{I} & \mathbf{0} & -b_4\mathbf{I} & \mathbf{I} & \mathbf{0} \\
\mathbf{0} & \mathbf{0} & \mathbf{0} & \mathbf{0} & \mathbf{0} & \mathbf{0} & \cdots & -b_1\mathbf{I} & -b_0\mathbf{I} & -\mathbf{I} & -b_2\mathbf{I} & \mathbf{0} & \mathbf{I}
\end{array}\right]. \tag{26}$$

While the description of the temporal discretization is well-known, we repeated the steps leading to eq. (23) to set the stage for the inverse source formulation, where eq. (23) is side-imposed to the objective functional to satisfy the underlying wave mechanics.

3 PARAMETRIZATION OF LOAD DESCRIPTORS

In our inverse source formulation, the search for the optimal source characteristics is carried out by an iterative scheme, following a reduced-space strategy. The formulation requires parametrization of the spatiotemporal load characteristics. To this end, the tractions $\mathbf{f}(\mathbf{x}, t)$ applied on Γ_{load} consist of contributions $\mathbf{f}_i(\mathbf{x}, t)$ from n_s sources, where $i = 1, \ldots, n_s$. The i-th source consists of a spatial $\theta_i(\mathbf{x})$ and a temporal $f_i(t)$ component. θ_i is further decomposed into the x_1-directional component $\theta_{i1}(\mathbf{x})$ and the x_2-directional component $\theta_{i2}(\mathbf{x})$. Thus,

$$\mathbf{f}(\mathbf{x}, t) = \sum_{i=1}^{n_s} \mathbf{f}_i(\mathbf{x}, t) = \sum_{i=1}^{n_s} \begin{bmatrix} \theta_{i1}(\mathbf{x}) \\ \theta_{i2}(\mathbf{x}) \end{bmatrix} f_i(t). \tag{27}$$

In our numerical experiments, we use loads in either the x_1 or x_2 direction, and therefore, either $\theta_{i1}(\mathbf{x}) = 0$ or $\theta_{i2}(\mathbf{x}) = 0$. We parametrize the (unknown) time signal using quadratic Lagrange polynomials $\tau_j(t)$ whose temporal nodal values are denoted by ξ_{ij}. This allows us to express $f_i(t)$ as

$$f_i(t) = \sum_{j=1}^{n_f} \xi_{ij}\tau_j(t), \tag{28}$$

where, n_f is the total number of the piecewise, narrowly supported, Lagrange polynomials. The spatial variation of the i-th load on Γ_{load} is captured by θ_{iK}, where subscript K describes the direction in which the load acts. In our experiments, we use a load varying like a Gaussian function in space, given by:

$$\theta_{iK}(x_1, 0) = -\exp\left[\frac{-(x_1 - \eta_i)^2}{b_i}\right], \tag{29}$$

where, η_i is the x_1 co-ordinate of the load's centre line and b_i controls the i-th load's width. We use (approximately) 2 m wide loads. Thus, for example, we set $b_i = 1.25\ \text{m}^2$ in eq. (29). We remark that other descriptions of spatial behaviour of loads can be easily accommodated in the formulation, for example, a constant pressure load applied vertically on part of the surface ($x_2 = 0$) can be expressed as,

$$\theta_{i2}(x_1, 0) = H\left(\eta_i - \frac{b_i}{2}\right) - H\left(\eta_i + \frac{b_i}{2}\right), \tag{30}$$

where, H is the Heaviside function. The necessary framework for formulation of the inverse source problem is now ready. In the next section, we present the formulation of the inverse problem.

4 THE INVERSE SOURCE PROBLEM

The inverse source problem aims at maximizing a predefined motion metric (e.g. the kinetic energy) of the target formation by seeking the optimal time signals and optimal locations for the surface tractions that are used to excite the computational/physical domain. The

problem can be cast as a constrained minimization problem, where maximization of a suitable objective functional is sought. The objective functional and the constraints can be cast in either their continuous or in their discrete form (Karve *et al.* 2014). In this work, we favour the latter approach, and begin the formulation with the fully discretized form (23) of the forward problem. The concept of discretizing first and then seeking to satisfy the optimality conditions (discretize-then-optimize) was first described in Gunzburger (2003), and results in the computation of consistent gradients. The objective functional is cast in its discrete form, as well. It is augmented by side-imposing the discrete governing equations, weighed by discrete Lagrange multipliers. To arrive at the KKT (Karush–Kuhn–Tucker) system, we then seek to satisfy the first-order optimality conditions. Herein, we choose an objective functional given by,

$$\mathcal{L}_d = \frac{1}{\rho_s \boldsymbol{u}^T \boldsymbol{B}_{in} \boldsymbol{u}} = \frac{1}{\rho_s\ \Delta t\ \left[\frac{1}{2}\dot{\mathbf{u}}_{\mathrm{a}_0}^T \dot{\mathbf{u}}_{\mathrm{a}_0} + \frac{1}{2}\dot{\mathbf{u}}_{\mathrm{a}_N}^T \dot{\mathbf{u}}_{\mathrm{a}_N} + \sum_{i=1}^{N-1} \dot{\mathbf{u}}_{\mathrm{a}_i}^T \dot{\mathbf{u}}_{\mathrm{a}_i}\right]}, \tag{31}$$

where, $\boldsymbol{B}_{in}$ is a block diagonal matrix with $\Delta t\, \boldsymbol{B}$ on its diagonal. $\boldsymbol{B}$ is a square matrix that is zero everywhere except on the diagonals that correspond to the $\dot{\mathbf{u}}_{\mathrm{a}}$ degrees-of-freedom. Thus, minimization of $\mathcal{L}_d$ is equivalent to maximization of the kinetic energy in the target, since $\mathcal{L}_d$ is the discrete version of the reciprocal of the time-integrated kinetic energy of the target's solid matrix ($\int_{\Omega_{\mathrm{a}}} \int_0^T \rho_s \dot{\mathbf{u}}_{\mathrm{a}} \cdot \dot{\mathbf{u}}_{\mathrm{a}}\, dt d\Omega$).

4.1 The Lagrangian

We side-impose the governing eqs (23), weighted by the discrete Lagrange multipliers $\boldsymbol{p}$, on the objective functional to obtain the discrete Lagrangian:

$$\mathcal{A}(\boldsymbol{u}, \boldsymbol{p}, \boldsymbol{f}) = \mathcal{L}_d - \boldsymbol{p}^T(\boldsymbol{Q}\boldsymbol{u} - \boldsymbol{f}). \tag{32}$$

Thus, the inverse problem can be stated as,

$$\min_f \quad \mathcal{A}(\boldsymbol{u}, \boldsymbol{p}, \boldsymbol{f}), \tag{33}$$

where,

$$\boldsymbol{p} = [\ddot{\boldsymbol{\lambda}}_0\ \dot{\boldsymbol{\lambda}}_0\ \boldsymbol{\lambda}_0\ \ddot{\boldsymbol{\lambda}}_1\ \dot{\boldsymbol{\lambda}}_1\ \boldsymbol{\lambda}_1\ \cdots\ \ddot{\boldsymbol{\lambda}}_N\ \dot{\boldsymbol{\lambda}}_N\ \boldsymbol{\lambda}_N\ ]^T, \tag{34}$$

$$\boldsymbol{\lambda} = \left[\boldsymbol{\lambda}_{w_1}\boldsymbol{\lambda}_{w_2}\boldsymbol{\lambda}_{u_{\mathrm{a}_1}}\boldsymbol{\lambda}_{u_{\mathrm{a}_2}}\middle|\boldsymbol{\lambda}_{u_{b_1}}^{\mathrm{reg}}\boldsymbol{\lambda}_{u_{b_2}}^{\mathrm{reg}}\middle|\boldsymbol{\lambda}_{u_{b_1}}^{\mathrm{PML}}\boldsymbol{\lambda}_{u_{b_2}}^{\mathrm{PML}}\boldsymbol{\lambda}_{S_{11}}\boldsymbol{\lambda}_{S_{22}}\boldsymbol{\lambda}_{S_{12}}\right]^T, \text{ with } \quad \boldsymbol{\lambda}_i \equiv \boldsymbol{\lambda}(i\Delta t). \tag{35}$$

The first-order optimality conditions are obtained by taking derivatives of $\mathcal{A}$ with respect to $\boldsymbol{u}$, $\boldsymbol{p}$ and $\boldsymbol{\lambda}$ and the source parameters ξ and η.

4.2 State problem

Differentiating $\mathcal{A}$ with respect to the Lagrange multipliers $\boldsymbol{p}$ yields:

$$\mathcal{A}_{\boldsymbol{p}}(\boldsymbol{u}, \boldsymbol{p}, \boldsymbol{f}) = \boldsymbol{0} \Rightarrow \boldsymbol{Q}\boldsymbol{u} = \boldsymbol{f}, \tag{36}$$

which is the same as the forward problem, given by eq. (23).[1]

4.3 Adjoint problem

Similarly, differentiating $\mathcal{A}$ with respect to the state variables $\boldsymbol{u}$ results in:

$$\mathcal{A}_{\boldsymbol{u}}(\boldsymbol{u}, \boldsymbol{p}, \boldsymbol{f}) = \boldsymbol{0} \Rightarrow -\boldsymbol{Q}^T\boldsymbol{p} - \frac{2\boldsymbol{B}_{in}\boldsymbol{u}}{\rho_s\ (\boldsymbol{u}^T\boldsymbol{B}_{in}\boldsymbol{u})^2} = \boldsymbol{0}. \tag{37}$$

Eq. (37) represents the *adjoint* problem associated with the inverse problem of interest. Since the adjoint problem involves the transpose of $\boldsymbol{Q}$, we solve it by marching backwards in time. From the last three rows of eq. (37), we get (for $i = N$),

$$\text{(update)}\ \ \boldsymbol{\lambda}_{\mathrm{N}} = \boldsymbol{\lambda}_N^{\mathrm{u}}, \tag{38a}$$

$$\text{(update)}\ \ \dot{\boldsymbol{\lambda}}_{\mathrm{N}} = \boldsymbol{\lambda}_N^{\mathrm{v}}, \tag{38b}$$

$$\text{(solve)}\ \ \mathbf{M}_{\mathrm{eff}}^T \ddot{\boldsymbol{\lambda}}_N = \boldsymbol{\lambda}_N^{\mathrm{a}} + b_4\dot{\boldsymbol{\lambda}}_N + b_2\boldsymbol{\lambda}_N. \tag{38c}$$

For $(N-1) \leq i \leq 1$, we update $\dot{\boldsymbol{\lambda}}_i$, $\boldsymbol{\lambda}_i$ and solve for $\ddot{\boldsymbol{\lambda}}_i$, as given by,

$$\text{(update)}\ \ \boldsymbol{\lambda}_i = \boldsymbol{\lambda}_i^{\mathrm{u}} + \boldsymbol{\lambda}_{i+1} - \mathbf{L}_0^T\ddot{\boldsymbol{\lambda}}_{i+1}, \tag{39a}$$

$$\text{(update)}\ \ \dot{\boldsymbol{\lambda}}_i = \boldsymbol{\lambda}_i^{\mathrm{v}} + b_0\boldsymbol{\lambda}_{i+1} + \dot{\boldsymbol{\lambda}}_{i+1} - \mathbf{L}_1^T\ddot{\boldsymbol{\lambda}}_{i+1}, \tag{39b}$$

[1] A subscript on the Lagrangian $\mathcal{A}$ denotes differentiation, that is, $\mathcal{A}_{\boldsymbol{p}} = \frac{\partial \mathcal{A}}{\partial \boldsymbol{p}}$.

$$\text{(solve)}\quad \mathbf{M}_{\text{eff}}^{T}\ddot{\boldsymbol{\lambda}}_i = \boldsymbol{\lambda}_i^{\text{a}} + b_1\boldsymbol{\lambda}_{i+1} + b_3\dot{\boldsymbol{\lambda}}_{i+1} - \mathbf{L}_2^{T}\ddot{\boldsymbol{\lambda}}_{i+1} + b_2\boldsymbol{\lambda}_i + b_4\dot{\boldsymbol{\lambda}}_i. \tag{39c}$$

For $i = 0$, we have,

$$\text{(solve)}\quad \mathbf{M}^{T}\ddot{\boldsymbol{\lambda}}_0 = \boldsymbol{\lambda}_0^{\text{a}} + b_1\boldsymbol{\lambda}_1 + b_3\dot{\boldsymbol{\lambda}}_1 - \mathbf{L}_2^{T}\ddot{\boldsymbol{\lambda}}_1, \tag{40a}$$

$$\text{(update)}\quad \boldsymbol{\lambda}_0 = \boldsymbol{\lambda}_0^{\text{u}} + \boldsymbol{\lambda}_1 - \mathbf{L}_0^{T}\ddot{\boldsymbol{\lambda}}_1 - \mathbf{K}^{T}\ddot{\boldsymbol{\lambda}}_0, \tag{40b}$$

$$\text{(update)}\quad \dot{\boldsymbol{\lambda}}_0 = \boldsymbol{\lambda}_0^{\text{v}} + b_0\boldsymbol{\lambda}_1 + \dot{\boldsymbol{\lambda}}_1 - \mathbf{L}_1^{T}\ddot{\boldsymbol{\lambda}}_1 - \mathbf{C}^{T}\ddot{\boldsymbol{\lambda}}_0. \tag{40c}$$

The vectors $\boldsymbol{\lambda}_i^{\text{u}}, \boldsymbol{\lambda}_i^{\text{v}}, \boldsymbol{\lambda}_i^{\text{a}}$, used in eqs (38)–(40), can be written as,

$$\boldsymbol{\lambda}_i^{\text{u}} = [\boldsymbol{\lambda}_{i,w}^{\text{u}}\ \boldsymbol{\lambda}_{i,u_{\text{a}}}^{\text{u}} \mid \boldsymbol{\lambda}_{i,u_b}^{\text{u}} \mid \boldsymbol{\lambda}_{i,u_b}^{\text{u}}\ \boldsymbol{\lambda}_{i,S}^{\text{u}}]^{T}, \tag{41a}$$

$$\boldsymbol{\lambda}_i^{\text{v}} = [\boldsymbol{\lambda}_{i,w}^{\text{v}}\ \boldsymbol{\lambda}_{i,u_{\text{a}}}^{\text{v}} \mid \boldsymbol{\lambda}_{i,u_b}^{\text{v}} \mid \boldsymbol{\lambda}_{i,u_b}^{\text{v}}\ \boldsymbol{\lambda}_{i,S}^{\text{v}}]^{T}, \tag{41b}$$

$$\boldsymbol{\lambda}_i^{\text{a}} = [\boldsymbol{\lambda}_{i,w}^{\text{a}}\ \boldsymbol{\lambda}_{i,u_{\text{a}}}^{\text{a}} \mid \boldsymbol{\lambda}_{i,u_b}^{\text{a}} \mid \boldsymbol{\lambda}_{i,u_b}^{\text{a}}\ \boldsymbol{\lambda}_{i,S}^{\text{a}}]^{T}, \tag{41c}$$

where we have grouped together the adjoint variables that correspond to the degrees-of-freedom within the target inclusion, regular domain and PML region. We obtain:

$$\boldsymbol{\lambda}_i^{\text{u}} = \boldsymbol{\lambda}_i^{\text{a}} = \mathbf{0},\ 0 \le i \le N, \tag{42a}$$

$$\boldsymbol{\lambda}_{i,w}^{\text{v}} = \mathbf{0}; \boldsymbol{\lambda}_{i,u_b}^{\text{v}} = \mathbf{0}; \boldsymbol{\lambda}_{i,S}^{\text{v}} = \mathbf{0};\ 0 \le i \le N, \tag{42b}$$

$$\boldsymbol{\lambda}_{i,u_{\text{a}}}^{\text{v}} = -\rho_s\ \Delta t\ \mathcal{L}_d^2\ \dot{\mathbf{u}}_{\text{a}_i},\ i = 0, N, \tag{42c}$$

$$\boldsymbol{\lambda}_{i,u_{\text{a}}}^{\text{v}} = -2\ \rho_s\ \Delta t\ \mathcal{L}_d^2\ \dot{\mathbf{u}}_{\text{a}_i},\ 0 < i < N. \tag{42d}$$

4.4 Control problem

4.4.1 Source time signal optimization

$$\mathcal{A}_{\xi_{mn}}(\boldsymbol{u}, \boldsymbol{p}, \boldsymbol{f}) = \boldsymbol{p}^{T}\frac{\partial \boldsymbol{f}}{\partial \xi_{mn}} = \sum_{i=0}^{N}\ddot{\boldsymbol{\lambda}}_i^{T}\frac{\partial \mathbf{F}_i}{\partial \xi_{mn}}, \tag{43}$$

is the gradient of the Lagrangian with respect to a given nodal-excitation parameter ξ_{mn}. For a load acting in the x_p direction, we update each element, ξ_{mn}, of the control parameter vector

$$\boldsymbol{\xi} = [\xi_{11}\ \xi_{12}\ \cdots\ \xi_{1n_f}\ \cdots\ \xi_{(n_s)(n_f-1)}\ \xi_{n_s n_f}], \tag{44}$$

using,

$$\begin{aligned}\mathcal{A}_{\xi_{mn}}(\boldsymbol{u}, \boldsymbol{p}, \boldsymbol{f}) &= \sum_{k=0}^{N}\ddot{\boldsymbol{\lambda}}_{k,\text{load}}^{T}\int_{\Gamma_{\text{load}}}\theta_{mp}(\mathbf{x})\Phi_u\ \tau_n(k\Delta t)\,d\Gamma \\ &= \sum_{k=0}^{N}\tau_n(k\Delta t)\,\ddot{\boldsymbol{\lambda}}_{k,\text{load}}^{T}\int_{\Gamma_{\text{load}}}\theta_{mp}(\mathbf{x})\Phi_u\,d\Gamma.\end{aligned} \tag{45}$$

4.4.2 Source location optimization

$$\mathcal{A}_{\eta_m}(\boldsymbol{u}, \boldsymbol{p}, \boldsymbol{f}) = \boldsymbol{p}^{T}\frac{\partial \boldsymbol{f}}{\partial \eta_m} = \sum_{i=0}^{N}\ddot{\boldsymbol{\lambda}}_i^{T}\frac{\partial \mathbf{F}_i}{\partial \eta_m}, \tag{46}$$

is the gradient of the Lagrangian with respect to a given load location parameter η_m. Thus, for a load acting in the x_p direction, we update each element, η_m, of the control parameter vector $\eta = \left[\eta_1\ \eta_2 \cdots \eta_{n_s}\right]$, using,

$$\begin{aligned}\mathcal{A}_{\eta_m}(\boldsymbol{u}, \boldsymbol{p}, \boldsymbol{f}) &= \sum_{k=0}^{N}\ddot{\boldsymbol{\lambda}}_{k,\text{load}}^{T}\int_{\Gamma_{\text{load}}}\frac{\partial\theta_{mp}}{\partial\eta_m}(\mathbf{x})\Phi_u\sum_{j=1}^{n_f}\xi_{mj}\tau_j(k\Delta t)\,d\Gamma, \\ &= \sum_{k=0}^{N}\left[\left(\sum_{j=1}^{n_f}\xi_{mj}\tau_j(k\Delta t)\right)\ddot{\boldsymbol{\lambda}}_{k,\text{load}}^{T}\int_{\Gamma_{\text{load}}}\frac{\partial\theta_{mp}}{\partial\eta_m}(\mathbf{x})\Phi_u\,d\Gamma\right].\end{aligned} \tag{47}$$

Table 2. Inversion algorithm.

Step 0		Choose an objective functional $\mathcal{L}$ Set value of tolerence *tol* Start with an *initial-guess* of $\boldsymbol{\xi} = \boldsymbol{\xi}_0$ and $\boldsymbol{\eta} = \boldsymbol{\eta}_0$, $(k = 0)$.
Step 1	(solve) (compute)	State problem $\mathcal{L}$ if $\mathcal{L} \leq tol$, *Convergence, STOP* else *GO TO Step 2*
Step 2	(solve)	Adjoint problem
Step 3		Control problem (update $\boldsymbol{\xi}$ and/or $\boldsymbol{\eta}$)
	(compute) (compute) (update)	Source time signal optimization: Gradient: $\mathbf{g}_{tk} = \mathcal{A}_{\xi_{mn}}(\boldsymbol{u}, \boldsymbol{p}, \boldsymbol{f})$ Search direction: $\mathbf{s}_{tk} = h(\mathbf{g}_{tk})$, $h : \mathbf{R}^p \rightarrow \mathbf{R}^p, \ p = dim(\boldsymbol{\xi})$ $\boldsymbol{\xi}_{k+1} = \boldsymbol{\xi}_k + \alpha_t \mathbf{s}_{tk}$
	(compute) (compute) (update)	Source location optimization: Gradient: $\mathbf{g}_{lk} = \mathcal{A}_{\eta_m}(\boldsymbol{u}, \boldsymbol{p}, \boldsymbol{f})$ Search direction: $\mathbf{s}_{lk} = h(\mathbf{g}_{lk})$, $h : \mathbf{R}^q \rightarrow \mathbf{R}^q, \ q = dim(\boldsymbol{\eta})$ $\boldsymbol{\eta}_{k+1} = \boldsymbol{\eta}_k + \alpha_l \mathbf{s}_{lk}$
	(update)	$k = k + 1$ *GO TO Step 1*

We remark that the gradient involves the derivative of the loading function θ. Since the derivative of a Heaviside function is a Dirac-delta function, the sharp variation in loading intensity given by eq. (30) requires impractically small element size on Γ_{load}. For this reason, we use eq. (29) to describe the spatial variability of loads for the inverse problems involving load location optimization.

4.5 Summary of the inversion process

Table 2 depicts the summary of the inversion process. We start with an initial guess for the load descriptors. We, then, solve the state problem and compute the objective functional. If the value of the objective functional is greater than the tolerance, the velocity vector in the target formation ($\dot{\mathbf{u}}_{a_i}$) is used to compute the body forces that drive the adjoint problem. Upon solution, the adjoint problem yields the values of the acceleration-like adjoint variable ($\ddot{\boldsymbol{\lambda}}_{i,\text{load}}$) that can be used to compute the gradients $\mathbf{g}_{tk}$ and $\mathbf{g}_{lk}$ (eqs 45 and 47). The function h is then used to compute the search directions. In this work, we used the search direction given by the conjugate gradient method. Step lengths α_t, α_l are used to update the source characteristics, and the procedure is repeated until convergence is reached.

5 NUMERICAL EXPERIMENTS

We evaluate the performance of the proposed method by conducting numerical experiments. We start our experiments with a guess for the locations and for the time signals of the surface loads. We, then, ask the optimizer to update the guess using the algorithm given in Table 2. It is known (Sánchez-Sesma *et al.* 2011) that a horizontally acting point load, applied on the surface of an elastic halfspace, imparts higher percentage of the input energy in terms of body waves than a vertically acting point load. A vertically acting point load expends about 65 per cent of its energy in the form of Rayleigh (surface) waves. In order to minimize the energy loss to surface motion, here we use horizontally acting surface loads, having maximum amplitude of 50 kN m^{-2}. The spatial description of loads is given by eq. (29). We remark that the procedure for optimizing vertically acting pressure loads is identical to that used for horizontal loads.

The geological formation models used in our numerical experiments are depicted in Fig. 2. They contain an elliptical, poroelastic target inclusion, having axes of lengths 30 m and 15 m. *P*- and *S*-wave speeds in the elastic formations are denoted by C_p and C_v, respectively. Other relevant material properties for the elastic solids are given in Tables 3 and 4. The properties of the poroelastic solid are given in Table 5. We use eight-noded, quadrilateral finite elements, and the time step for temporal discretization is set at $\Delta t = 0.001$ s. We use the time-averaged kinetic energy ($\text{KE}_{\text{TA, s}}$) at a node, measured in J m^{-1} and the time-averaged kinetic energy ($\text{KE}_{\text{inc, s}}$), integrated over the target formation, as

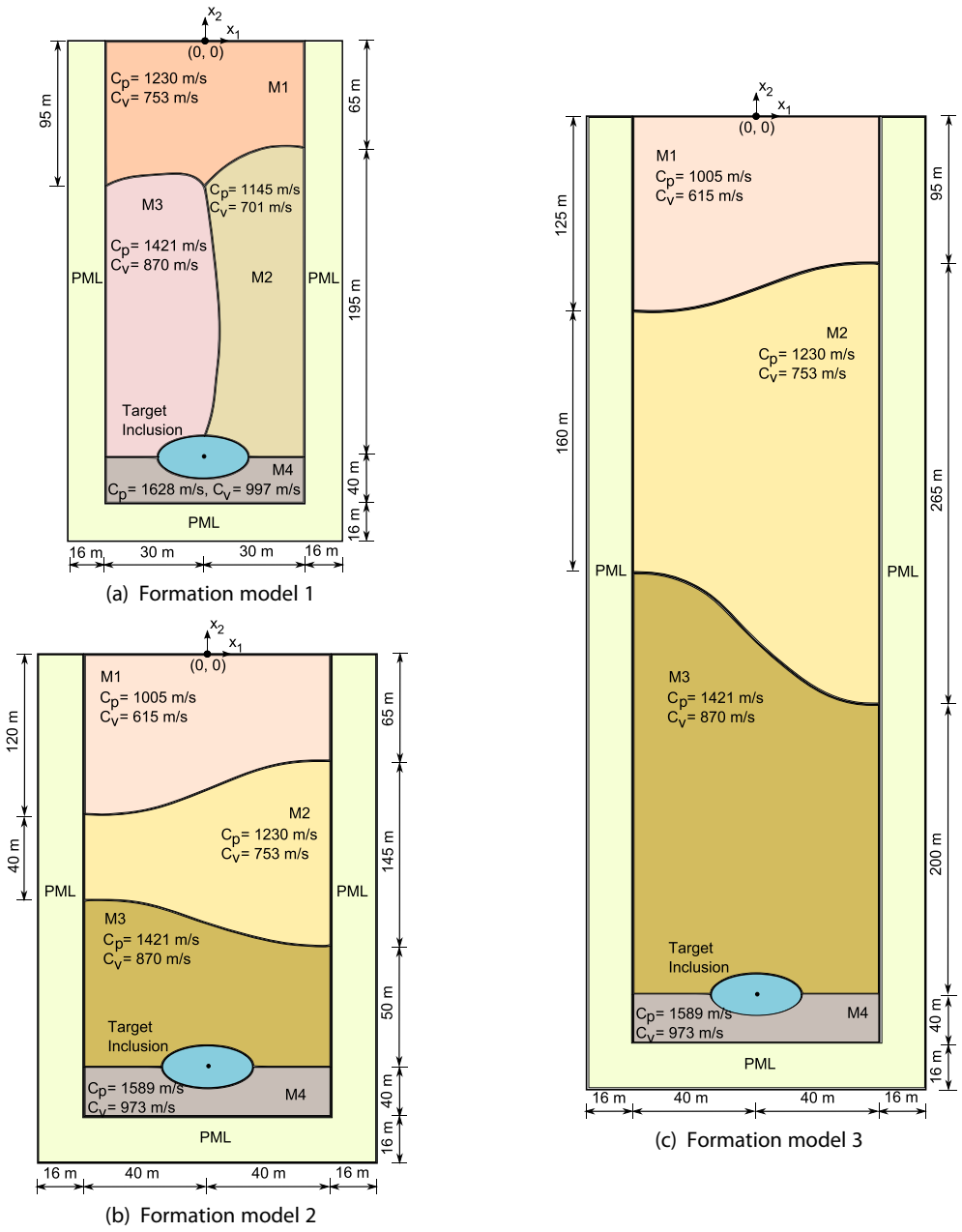

Figure 2. Geological formation models for numerical experiments.

Table 3. Formation model 1 material properties.

Material ID	C_p (m s^{-1})	C_v (m s^{-1})	ρ_s (kg m^{-3})
M1	1230	753	2200
M2	1145	701	2200
M3	1421	870	2200
M4	1628	997	2200

Table 4. Formation models 2 and 3 material properties.

Material ID	C_p (m s^{-1})	C_v (m s^{-1})	ρ_s (kg m^{-3})
M1	1005	615	2200
M2	1230	753	2200
M3	1421	870	2200
M4	1589	973	2200

Table 5. Poroelastic inclusion properties for formation models 1, 2 and 3.

K_a (GPa)	G_a (GPa)	K_f (GPa)	ρ_a (kg m^{-3})	ρ_f (kg m^{-3})	ϕ	α	μ (kg (ms)$^{-1}$)	k (Darcy)
0.556	0.412	2	1865	860	0.25	0.75	0.0025	0.5

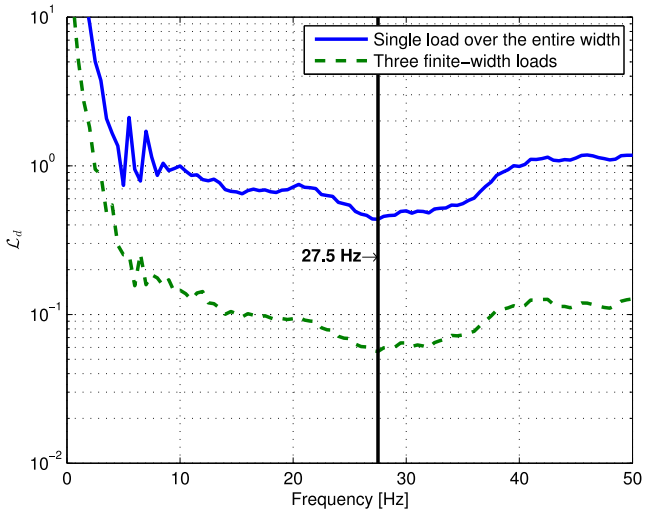

Figure 3. Frequency sweep results—geological formation model 1.

performance metrics of the developed algorithm:

$$\mathrm{KE}_{\mathrm{TA,s}} = \int_0^T \frac{1}{2}\rho_s\,[\dot{\mathbf{u}}(t)\cdot\dot{\mathbf{u}}(t)]\,dt \;\Big/ T, \tag{48}$$

$$\mathrm{KE}_{\mathrm{inc,s}} = \int_{\Omega_a}\int_0^T \frac{1}{2}\rho_s\,[\dot{\mathbf{u}}_a\cdot\dot{\mathbf{u}}_a]\,dt\,d\Omega \;\Big/ T = \int_0^T \frac{1}{2}\rho_s\,\dot{\mathbf{u}}_a(t)^T\mathbf{M}^a_{uu}\dot{\mathbf{u}}_a(t)dt \;\Big/ T, \tag{49}$$

where, $\dot{\mathbf{u}}_a(t)$ is the solid's velocity vector corresponding to the computational nodes in the inclusion and $\mathbf{M}^a_{uu}$ is the mass matrix of the target inclusion (see Appendix B for the definition). To illustrate, we consider candidate pores whose axes make an angle of 60 deg with the x_1 axis. We calculate the maximum and minimum fluid accelerations with respect to the walls of these pores, as

$$a_{\mathrm{f,max}} = \max_{\Omega_a}\left[\frac{|\ddot{w}_1(t)\cos(\pi/3)+\ddot{w}_2(t)\sin(\pi/3)|}{\phi}\right], \tag{50}$$

$$a_{\mathrm{f,min}} = \min_{\Omega_a}\left[\frac{|\ddot{w}_1(t)\cos(\pi/3)+\ddot{w}_2(t)\sin(\pi/3)|}{\phi}\right]. \tag{51}$$

We remark that the choice of pore orientation (60 deg) is arbitrary. The fluid acceleration for different pore orientations can be computed if a statistical measure of the acceleration corresponding to a realistic distribution of pore orientations is desired. Next, we report the results of the source time signal and/or source location optimization.

5.1 Experiment 1

We begin the experiment by comparing two methodologies used to decide the optimal frequency content of the time signals driving the loads: a frequency sweep approach (if interested in monochromatic loads only), and the inverse source algorithm described earlier. The frequency sweep, which involves computing the objective functional over a predetermined range of frequencies, can be carried out for: (i) a load acting on the entire width of the computational domain, or (ii) a number of finite-width loads placed at fixed (guessed) locations; the aim is to probe the formation's intrinsic dynamic properties. We use the geological formation model 1 and horizontally polarized loads to compare the results of both these approaches. The simulations are performed for a total time $T = 1.5$ s. For the frequency sweep with a single uniform load, the entire width of the computational domain is subjected to a horizontal load, and the amplitude of the sine function is set at 2 kN m^{-2}. For the case of finite-width loads, we place three loads, having a width of approximately 2 m, at fixed locations (0, 0)m, (−7, 0)m and (5, 0)m. The amplitude of the monochromatic sine function is set at 50 kN m^{-2}. Fig. 3 shows the results of the sweeps. For the range of frequencies considered, a global minimum for the reciprocal of the target's kinetic energy occurs, approximately, at 27.5 Hz for both cases; this value corresponds to one of the formation's amplification frequencies.

Next, we perform the time signal optimization using the inverse source algorithm outlined in Table 2. We place three horizontal loads at (0, 0)m, (−7, 0)m and (5, 0)m. The spatial description of the loads is given by eq. (29). The initial guess of the time signals is shown in

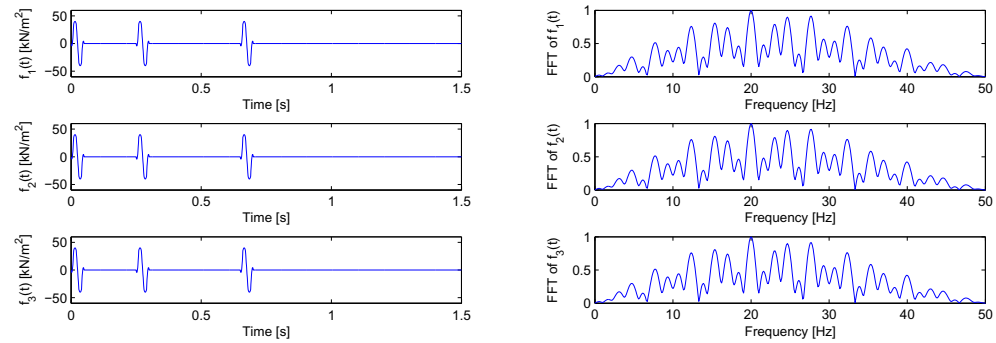

(a) Initial guess

(b) Frequency spectra of initial guess

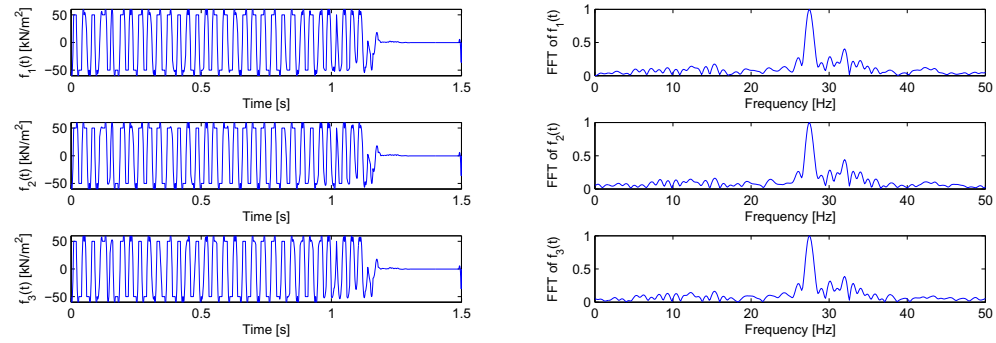

(c) Converged time signals (after time signal optimization)

(d) Frequency spectra of converged time signals (after time signal optimization)

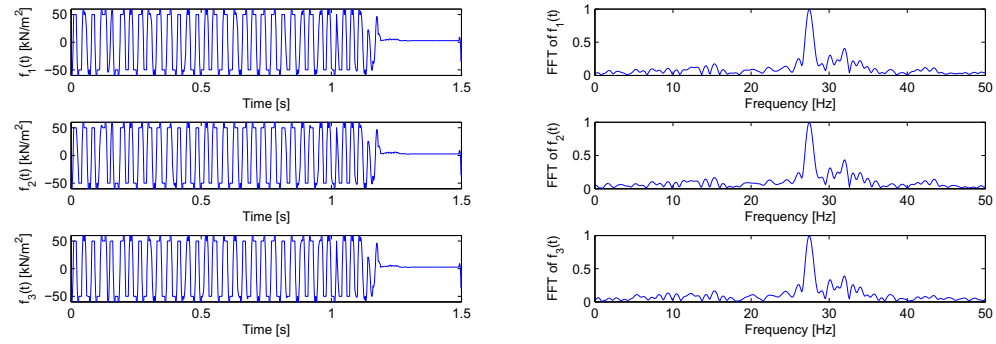

(e) Converged time signals (after time signal and load location optimization)

(f) Frequency spectra of converged time signals (after time signal and load location optimization)

Figure 4. Experiment 1—time signals and frequency spectra.

Fig. 4(a). The initial guess contains a broad range of frequencies (Fig. 4b). The converged time signals and their frequency spectra are shown in Figs 4(c) and (d), respectively. The optimizer converges on near-monochromatic time signals having 27.5 Hz as the dominant frequency. The $KE_{inc,s}$ for the converged time signals is $0.90\,J\,m^{-1}$. The plot of $KE_{TA,s}$ is shown in Fig. 5(b). The fact that the optimizer converged to a near-monochromatic signal having a frequency equal to the one obtained by the frequency sweep provides a validation for the inverse source approach.

We next compare the results obtained by the inverse source approach when seeking to optimize the time signals of fixed-location sources versus those obtained when seeking to simultaneously optimize source time signals and source locations. To this end, we begin the simultaneous optimization process (Table 2) with the same initial guesses of signals and locations as those used for the time signal optimization case with fixed locations. The converged, near-monochromatic time signals, exhibiting the dominant frequency of 27.5 Hz, are shown in Fig. 4(e). Fig. 5(c) shows the plot of $KE_{TA,s}$. The $KE_{inc,s}$ achieved by the simultaneous signal-location optimization process is $1.26\,J\,m^{-1}$.

The experiment highlights the importance of the load locations. For the short computational time of 1.5 s used in our experiment, the loads placed at optimal locations were able to deliver 38 per cent more time-averaged kinetic energy to the target than the blindly placed sources. In a field implementation of seismic EOR, where stimulation may be applied for days or even weeks at a time, the difference amounts to a significant increase in efficiency.

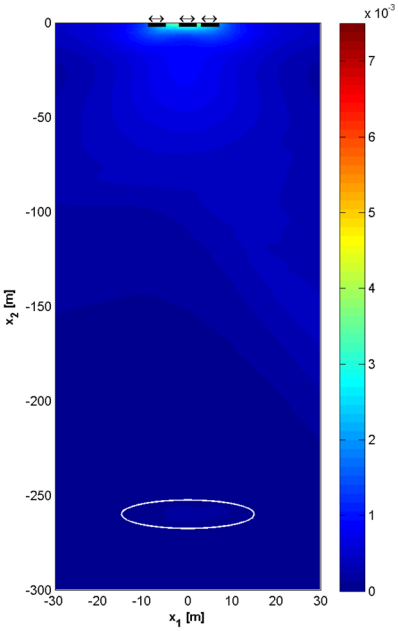

(a) $\mathrm{KE}_{\mathrm{TA,s}}$ for the initial guess of time signals; loads fixed at (-7,0)m, (0,0)m, and (5,0)m

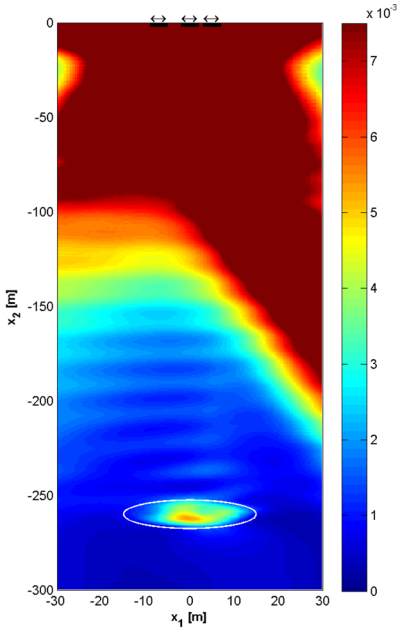

(b) $\mathrm{KE}_{\mathrm{TA,s}}$ after time signal optimization only; loads fixed at (-7,0)m, (0,0)m, and (5,0)m

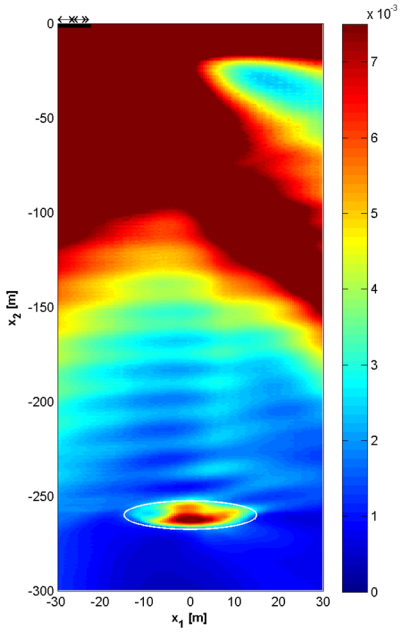

(c) $\mathrm{KE}_{\mathrm{TA,s}}$ after time signal and load location optimization; load locations converged to (-25.17,0)m, (-24.48,0)m, and (-28.15,0)m

Figure 5. Experiment 1—time-averaged kinetic energy.

5.2 Experiment 2

In this experiment, we use formation model 2 and perform simultaneous time signal and load location optimization. We use six horizontally acting surface loads to simulate the action of a fleet of Vibroseis actuators. The initial guess and converged values of the time signals are shown in Fig. 6. Fig. 7 depicts the time-averaged kinetic energy $\mathrm{KE}_{\mathrm{TA,s}}$ before and after the optimization process. The initial and converged locations of loads are given in Table 6. It can be seen from the converged load locations that the optimizer tried to arrange the loads in three groups centred at, approximately, $(-26, 0)$m, $(-2, 0)$m and $(-37, 0)$m. The optimizer is able to deliver a $\mathrm{KE}_{\mathrm{inc,s}}$ of $14.61\,\mathrm{J\,m^{-1}}$. As it can

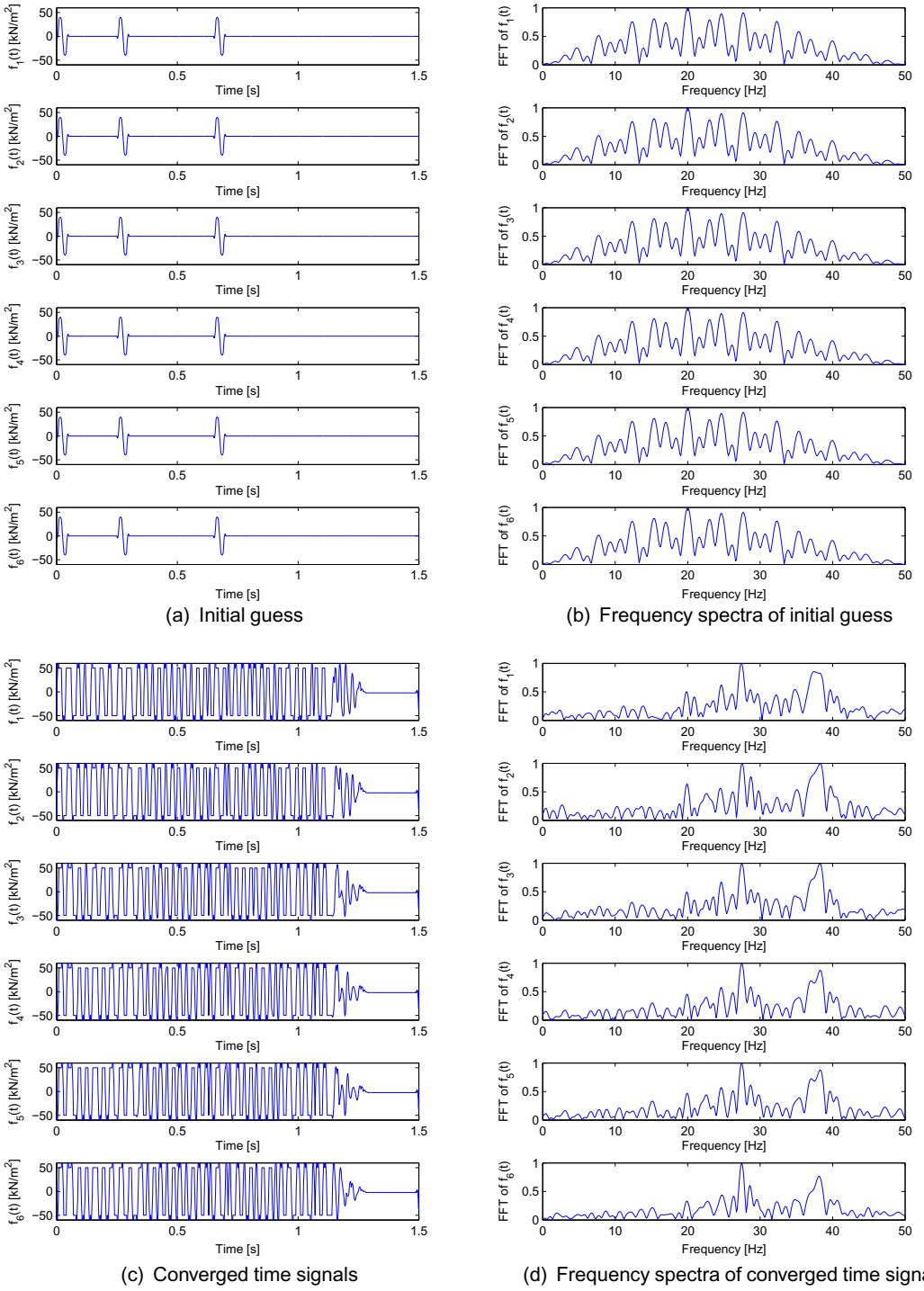

Figure 6. Experiment 2—time signals and frequency spectra.

be seen in Fig. 6, this time, the spectra of the converged signals have a rich content, accounting not only for the dominant amplification frequencies of the formation but also for the complex propagation paths arising in the particular formation.

5.3 Experiment 3

Here, we use the deeper geological formation model 3 to perform simultaneous time signal and load location optimization. Note that the target inclusion for the formation model 3 is located at about 550 m below the ground level, or otherwise, at a depth that is about twice that of the target inclusion in formation model 2. Once again, we use six horizontally polarized loads to simulate the action of a fleet of Vibroseis trucks. The experiment is performed for a total simulation time $T = 2$ s. The initial guess and converged values of the time signals are shown in Fig. 8. Table 7 lists the load locations before and after the optimization. Fig. 9 depicts the distribution of $\mathrm{KE}_{\mathrm{TA,s}}$. $\mathrm{KE}_{\mathrm{inc,s}}$ for Fig. 9(b) is $4.32\,\mathrm{J\,m^{-1}}$.

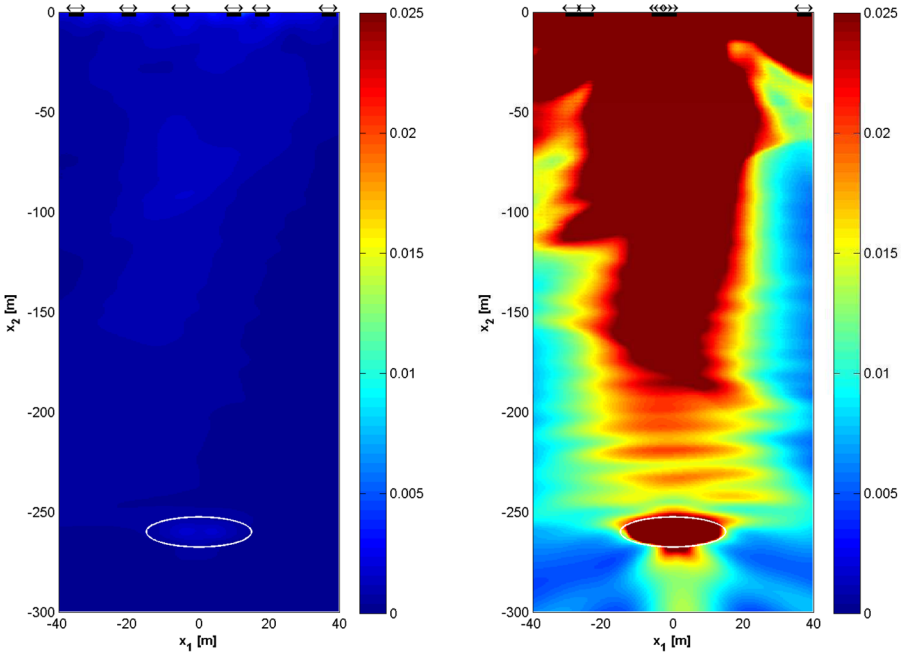

(a) $\mathrm{KE}_{\mathrm{TA,s}}$ for the initial guess of time signals and load locations

(b) $\mathrm{KE}_{\mathrm{TA,s}}$ after optimization

Figure 7. Experiment 2—time-averaged kinetic energy.

Table 6. Load locations for experiment 2.

Load number	Initial locations (m,m)	Converged locations (m,m)
1	(−35.00, 0)	(−28.65, 0)
2	(−20.00, 0)	(−24.61, 0)
3	(−5.00, 0)	(−4.05, 0)
4	(10.00, 0)	(−1.08, 0)
5	(18.00, 0)	(−2.67, 0)
6	(37.00, 0)	(37.41, 0)

5.4 Experiment 4

In the preceding numerical experiments, we assumed that the material properties of the layers are known with confidence. In practice, however, the knowledge about the material properties and the geometric description of the geostructure in question is imperfect. To illustrate the effect of the material uncertainties on the intensity of wave energy focusing, we conduct a simple numerical test.

In experiment 2, we resolved the inverse source problem for geological formation model 2 endowed with material properties given in Tables 4 and 5. Here, we assume that the properties used in that experiment were 'incorrect' and that the 'correct' material properties are those given in Tables 8 and 9. The difference between (K_{a}, G_{a}) and (K_{b}, G_{b}) values of the 'correct' and 'incorrect' profiles ranges between 12 and 50 per cent. We use the spatiotemporally optimized loads computed in experiment 2 (Figs 6c and d and Table 6) to excite the geological formation model 2 endowed with the presumed 'correct' material properties. Fig. 10 shows the distribution of $\mathrm{KE}_{\mathrm{TA,s}}$. The $\mathrm{KE}_{\mathrm{inc,s}}$ value is reduced by about 50 per cent from 14.69 to 7.51 J m^{-1}. Thus, the uncertainties in the knowledge of the material properties tend to reduce the amount of the kinetic energy delivered to the target, but the focusing appears to remain intact.

The effect of uncertainty in the input geometric and material data on the energy delivery to the target formation can be systematically evaluated using sensitivity and uncertainty analyses. The sensitivity analysis can be used to compute the derivative of $\mathrm{KE}_{\mathrm{inc,s}}$ with respect to a given material property of a layer. Moreover, the material properties can be treated as random variables described by suitable probability distribution functions (PDFs), and the probability of failure to achieve a given $\mathrm{KE}_{\mathrm{inc,s}}$ value can be computed using a formal uncertainty analysis. These analyses can aid the engineering and economic decision making process for the field implementation of the wave-based EOR method. A detailed discussion of these methodologies is beyond the scope of this article.

The results of our numerical experiments are summarized in Table 10, where we report the values of maximum and minimum fluid accelerations, along with the values of $\mathrm{KE}_{\mathrm{inc,s}}$, and other characteristics of our numerical experiments. In experiment 1, we compared the results of time signal optimization with those of simultaneous signal-location optimization. The simultaneous optimization procedure was able to deliver about 38 per cent more $\mathrm{KE}_{\mathrm{inc,s}}$ to the target than the time signal optimization. Furthermore, the fluid accelerations $a_{\mathrm{f,\,max}}$ and $a_{\mathrm{f,\,min}}$

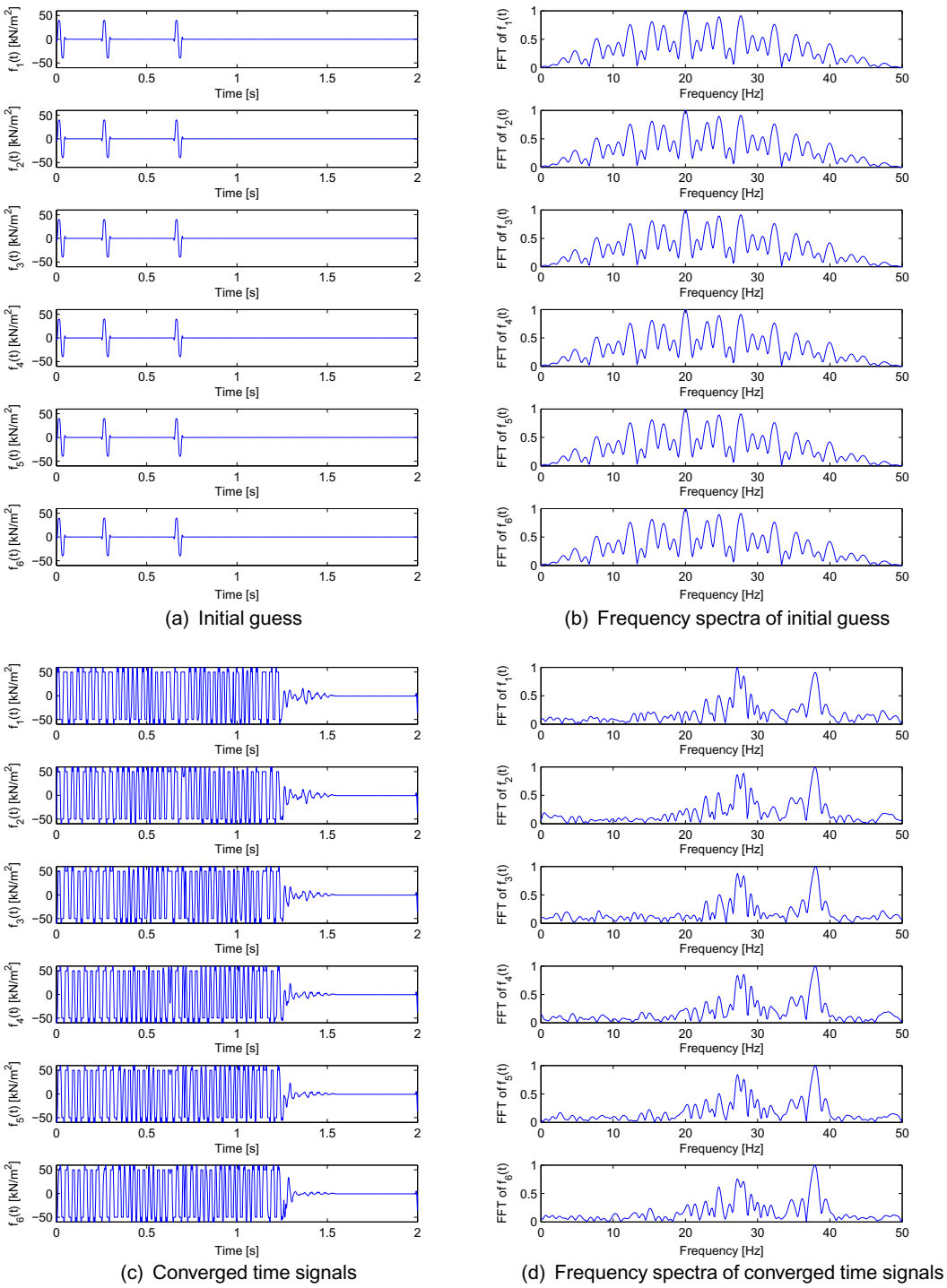

Figure 8. Experiment 3—time signals and frequency spectra.

(eqs 50 and 51) for the case of the simultaneous optimization, are about two times greater than those for corresponding the time-signal-only optimization case. This experiment highlights the importance of placing loads at optimal locations, especially in the case of geological formations exhibiting a high degree of heterogeneity. Experiments 2 and 3 were conducted to observe the effect of depth of the target on the energy focusing and the magnitude of the fluid acceleration field. The $KE_{inc,s}$ for the deeper target is about three times lower than that for the shallower target. The minimum and maximum acceleration values are reduced by a factor of two for the deeper target. But, more importantly, in both cases the inverse source optimizer arrived at source characteristics, which successfully illuminated the target formation, independent of the target's depth.

Table 7. Load locations for experiment 3.

Load number	Initial locations (m,m)	Converged locations (m,m)
1	(−35.00, 0)	(−33.88, 0)
2	(−20.00, 0)	(−24.12, 0)
3	(−5.00, 0)	(−7.53, 0)
4	(10.00, 0)	(6.64, 0)
5	(18.00, 0)	(14.53, 0)
6	(37.00, 0)	(37.91, 0)

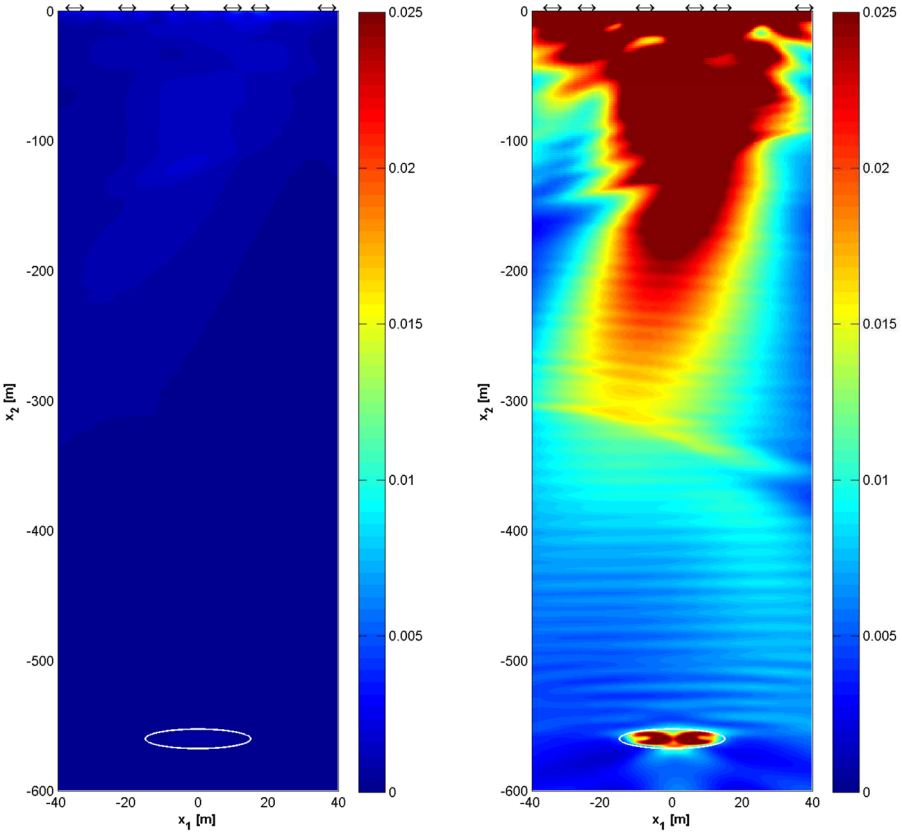

(a) $\mathrm{KE}_{\mathrm{TA,s}}$ for the initial guess of time signals and load locations

(b) $\mathrm{KE}_{\mathrm{TA,s}}$ after optimization

Figure 9. Experiment 3—time-averaged kinetic energy.

Table 8. 'Correct' elastic material properties for formation model 2.

Material ID	C_p (m s^{-1})	C_v (m s^{-1})	ρ_s (kg m^{-3})
M1	1066	652	2200
M2	1348	825	2200
M3	1524	933	2200
M4	1666	1020	2200

Table 9. 'Correct' poroelastic inclusion properties for formation model 2.

K_a (GPa)	G_a (GPa)	K_f (GPa)	ρ_a (kg m^{-3})	ρ_f (kg m^{-3})	ϕ	α	μ (kg (ms)$^{-1}$)	k (Darcy)
0.833	0.625	2	1865	860	0.25	0.69	0.0025	0.5

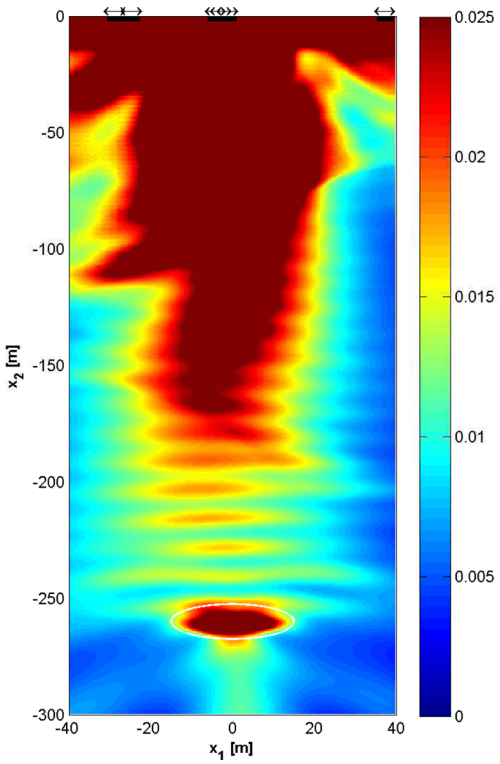

Figure 10. Experiment 4—$KE_{TA,\,s}$ for geological formation model 2 endowed with the 'correct' material properties.

Table 10. Summary of numerical experiments.

Numerical experiment number	Formation model number	Loading direction	Control variable(s)	$KE_{inc,\,s}$ ($J\,m^{-1}$)	$a_{f,\,max}$ ($mm\,s^{-2}$)	$a_{f,\,min}$ ($mm\,s^{-2}$)
1	1	Horizontal	Time signal	0.90	5.16	1.03
		Horizontal	Time signal and load location (simultaneously)	1.26	10.20	1.93
2	2	Horizontal	Time signal and load location (simultaneously)	14.61	6.51	0.99
3	3	Horizontal	Time signal and load location (simultaneously)	4.32	2.95	0.53

6 EXTENSIONS

In this section, we discuss the formulation for an objective functional constructed using a measure of the input energy in addition to the metric of motion in the target inclusion. We use the inner product of nodal forces and nodal displacements on the loaded portion of the free surface to estimate the input energy. Consider the vector $\tilde{\boldsymbol{f}}$, given by,

$$\tilde{\boldsymbol{f}} = \Delta t[\mathbf{0}\ \mathbf{0}\ \mathbf{F}_0\ \mathbf{0}\ \mathbf{0}\ \mathbf{F}_1\ \cdots\ \mathbf{0}\ \mathbf{0}\ \mathbf{F}_N]^T. \tag{52}$$

Thus, the inner product,

$$\boldsymbol{u}^T\tilde{\boldsymbol{f}} = \Delta t\,\mathbf{d}_0^T\mathbf{F}_0 + \Delta t\,\mathbf{d}_1^T\mathbf{F}_1 + \cdots + \Delta t\,\mathbf{d}_N^T\mathbf{F}_{\mathrm{N}}, \tag{53}$$

can be used as a measure of the time-integrated input energy. A search for load characteristics that maximize the motion within the target inclusion, while minimizing the input energy metric can now be conducted by defining an objective functional, $\mathcal{L}_{d_1}$ as:

$$\mathcal{L}_{d_1} = \frac{\boldsymbol{u}^T\tilde{\boldsymbol{f}}}{\rho_s\boldsymbol{u}^T\boldsymbol{B}_{in}\boldsymbol{u}} = \left(\boldsymbol{u}^T\tilde{\boldsymbol{f}}\right)\mathcal{L}_d. \tag{54}$$

For the inverse source problem cast using $\mathcal{L}_{d_1}$, the state problem is still given by eq. (23). The adjoint problem changes to

$$-\boldsymbol{Q}^T\boldsymbol{p} - \frac{2\boldsymbol{B}_{in}\boldsymbol{u}}{\rho_s\,(\boldsymbol{u}^T\boldsymbol{B}_{in}\boldsymbol{u})^2} + \frac{\tilde{\boldsymbol{f}}}{\rho_s\,(\boldsymbol{u}^T\boldsymbol{B}_{in}\boldsymbol{u})} = \mathbf{0}. \tag{55}$$

The modified control equations are given by:

$$\mathcal{A}_{\xi_{mn}}(\boldsymbol{u},\,\boldsymbol{p},\,\boldsymbol{f}) = \sum_{k=0}^{N}\tau_n(k\Delta t)\,\left(\ddot{\boldsymbol{\lambda}}_{k,\mathrm{load}}^T + \Delta t\mathcal{L}_d\mathbf{u}_{k,\mathrm{load}}^T\right)\int_{\Gamma_{\mathrm{load}}}\theta_{mp}(\mathbf{x})\Phi_u\,d\Gamma, \tag{56}$$

and

$$\mathcal{A}_{\eta_m}(\boldsymbol{u},\,\boldsymbol{p},\,\boldsymbol{f}) = \sum_{k=0}^{N}\left[\left(\sum_{j=1}^{n_f}\xi_{mj}\tau_j(k\Delta t)\right)\left(\ddot{\boldsymbol{\lambda}}_{k,\mathrm{load}}^T + \Delta t\mathcal{L}_d\mathbf{u}_{k,\mathrm{load}}^T\right)\int_{\Gamma_{\mathrm{load}}}\frac{\partial\theta_{mp}}{\partial\eta_m}(\mathbf{x})\Phi_u\,d\Gamma\right]. \tag{57}$$

Functional (54) can be used when the interest is in maximizing energy delivery at the target formation, while expending minimal input energy. We remark that the numerator of (54) can be replaced by more suitable definitions of input energy reflecting the equipment's actual energy expenditure. We also note that other target motion metrics can be accommodated by merely changing of the definition of $\mathcal{L}_d$.

7 CONCLUSIONS

We presented an inverse source problem formulated for focusing wave energy to subterranean poroelastic formations. The developed approach offers an important analytical tool for quantifying the strength of vibrations imparted to the particles trapped in the narrow pores of geological formations. This analysis, in conjunction with pore-scale simulations, facilitates the design of field implementations of wave-based EOR methods.

The inverse source problem deals with reservoir-scale wave propagation and seeks the optimal locations and temporal descriptions for the surface loads, where optimality is defined based on the maximization of a desired motion metric within the reservoir. We formulated the underlying wave physics in two spatial dimensions. The reservoir was abstracted as a poroelastic solid using Biot's equations, and elastic behaviour was assumed for formations surrounding the reservoir. The semi-infinite nature of the governing wave propagation was negotiated using computationally efficient, hybrid PMLs. The optimization problem was cast for the field equations in their discretized form, instead of their continuous form. Numerical experiments were conducted to determine the effectiveness of the proposed technique.

Our experiments suggest that optimal load locations of surface loads play a critical role in maximizing energy delivery to the target formation. The optimizer is capable of arriving at source characteristics that successfully produce conditions of constructive interference at the target, thus illuminating the formation. For the 2-D setting adopted in our numerical experiments, we computed that the acceleration of fluid particles with respect to the solid matrix (pore walls) ranges between 1–10 mm s^{-2}. The magnitude of the acceleration may be increased by applying surface loads of higher amplitudes or by increasing the number of loads used. We remark, however, that the reported acceleration levels may still lead to trapped particle release by one of the mechanisms discussed in Kurlenya & Serdyukov (1999), Kostrov & Wooden (2002), Roberts & Abdel-Fattah (2009) and Beresnev *et al.* (2011).

ACKNOWLEDGEMENTS

The authors' work was partially supported by an Academic Excellence Alliance grant between the King Abdullah University of Science and Technology in Saudi Arabia (KAUST) and the University of Texas at Austin. The support is gratefully acknowledged.

REFERENCES

Bamberger, A., Chavent, G. & Lailly, P., 1979. About the stability of the inverse problem in 1-D wave equations–application to the interpretation of seismic profiles, *Appl. Math. Optim.,* **5**(1), 1–47.

Beresnev, I., Gaul, W. & Vigil, R.D., 2011. Direct pore-level observation of permeability increase in two-phase flow by shaking, *Geophys. Res. Lett.,* **38**(20), L20302, doi:10.1029/2011GL048840.

Beresnev, I.A. & Deng, W., 2010. Viscosity effects in vibratory mobilization of residual oil, *Geophysics,* **75**(4), N79–N85.

Beresnev, I.A. & Johnson, P.A., 1994. Elastic-wave stimulation of oil production: A review of methods and results, *Geophysics,* **59**(6), 1000–1017.

Biot, M.A., 1956. Theory of propagation of elastic waves in a fluid saturated porous solid.I. low frequency range, *J. acoust. Soc. Am.,* **28**(2), 168–178.

Bourbié, T., Coussy, O. & Zinszer, B., 1987. *Acoustics of Porous Media,* Gulf Publishing Company.

Bunks, C., Saleck, F., Zaleski, S. & Chavent, G., 1995. Multiscale seismic waveform inversion, *Geophysics,* **60**(5), 1457–1473.

Deng, W. & Cardenas, M.B., 2013. Dynamics and dislodgment from pore constrictions of a trapped nonwetting droplet stimulated by seismic waves, *Water Resour. Res.,* **49**(7), 4206–4218.

Epanomeritakis, I., Akçelik, V., Ghattas, O. & Bielak, J., 2008. A Newton-CG method for large-scale three-dimensional elastic full-waveform seismic inversion, *Inverse Probl.,* **24**(3), 034015, doi:10.1088/0266-5611/24/3/034015.

Gunzburger, M.D., 2003. *Perspectives in Flow Control and Optimization,* SIAM.

IEO, 2013. *International Energy Outlook,* U.S. Energy Information Administration.

Jeong, C., Huh, C. & Kallivokas, L.F., 2011a. On the feasibility of inducing oil mobilization in existing reservoirs via wellbore harmonic fluid action, *J. Petrol. Sci. Eng.,* **76**(3–4), 116–123.

Jeong, C., Kallivokas, L.F., Huh, C. & Lake, L.W., 2011b. Maximization of oil mobility within a hydrocarbon reservoir for elastic wave-based enhanced oil recovery, in *SPE Annual Technical Conference and Exhibition, SPE 147150,* Society of Petroleum Engineers.

Kallivokas, L., Fathi, A., Kucukcoban, S., Stokoe, K., II Bielak, J. & Ghattas, O., 2013. Site characterization using full waveform inversion, *Soil Dyn. Earthq. Eng.,* **47**(0), 62–82.

Karve, P.M., Kucukcoban, S. & Kallivokas, L.F., 2014. On an inverse source problem for enhanced oil recovery by wave motion maximization in reservoirs, *Comput. Geosci.,* doi:10.1007/s10596-014-9462-7.

Kostrov, S.A. & Wooden, B.O., 2002. Mechanisms, field suitability, and case studies for enhancement of oil recovery and production using in-situ seismic stimulation, in *16th International Symposium on Nonlinear Acoustics,* Moscow, Russia.

Kucukcoban, S. & Kallivokas, L., 2013. A symmetric hybrid formulation for transient wave simulations in pml-truncated heterogeneous media, *Wave Motion,* **50**(1), 57–79.

Kurlenya, M. & Serdyukov, S., 1999. Reaction of fluids of an oil-producing stratum to low-intensity vibro-seismic action, *J. Min. Sci.,* **35**(2), 113–119.

Lake, L., 1989. *Enhanced Oil Recovery,* Prentice Hall Incorporated.

Manga, M., Beresnev, I., Brodsky, E.E., Elkhoury, J.E., Elsworth, D., Ingebritsen, S.E., Mays, D.C. & Wang, C.-Y., 2012. Changes in permeability caused by transient stresses: field observations, experiments, and mechanisms, *Rev. Geophys.,* **50**(2), doi:10.1029/2011RG000382.

Roberts, P.M. & Abdel-Fattah, A.I., 2009. Seismic stress stimulation mobilizes colloids trapped in a porous rock, *Earth planet. Sci. Lett.,* **284**(3), 538–543.

Sánchez-Sesma, F.J., Weaver, R.L., Kawase, H., Matsushima, S., Luzón, F. & Campillo, M., 2011. Energy partitions among elastic waves for dynamic surface loads in a semi-infinite solid, *Bull. seism. Soc. Am.,* **101**(4), 1704–1709.

Schanz, M., 2009. Poroelastodynamics: linear models, analytical solutions, and numerical methods, *Appl. Mech. Rev.,* **62**(3), doi:10.1115/1.3090831.

Smimova, M.N., 1968. Effect of eartquakes on the yield of Gudermes field (Northeastern Caucasus), *Fizika Zemli (Physics of the Solid Earth),* **12,** 71–75.

Steinbrugge, K.V. & Moran, D.F., 1954. An engineering study of the Southern California earthquake of July 21, 1952 and its aftershocks, *Bull. seism. Soc. Am.,* **44**(2B), 201–462.

Tarantola, A., 1984. Inversion of seismic reflection data in the acoustic approximation, *Geophysics,* **49**(8), 1259–1266.

Voitov, G., Osika, G., Plotniko, I. & Grechukh, T., 1972. Some geologic-geochemical consequences of Dagestan earthquake of May 14, 1970, *Doklady Akademii nauk SSSR,* **202**(3), 576–579.

APPENDIX A: CONTROL PROBLEM DERIVATION

A1 Source time signal optimization

Consider the derivative of $\mathcal{A}$, with respect to the nodal-excitation parameter ξ_{mn},

$$\mathcal{A}_{\xi_{mn}}(\boldsymbol{u},\, \boldsymbol{p},\, \boldsymbol{f}) = \sum_{i=0}^{N} \ddot{\boldsymbol{\lambda}}_i^T \frac{\partial \mathbf{F}_i}{\partial \xi_{mn}}. \tag{A1}$$

We recall that, for each element,

$$\mathbf{F}_k^{\text{elem}} = \sum_{i=1}^{n_s} \int_{\Gamma_{\text{load}}} \begin{bmatrix} \theta_{i1}(\mathbf{x})\Phi_u \\ \theta_{i2}(\mathbf{x})\Phi_u \end{bmatrix} \sum_{j=1}^{n_f} \xi_{ij}\tau_j(k\Delta t)\, d\Gamma,$$

$$\frac{\partial \mathbf{F}_k^{\text{elem}}}{\partial \xi_{mn}} = \int_{\Gamma_{\text{load}}} \begin{bmatrix} \theta_{m1}(\mathbf{x})\Phi_u \\ \theta_{m2}(\mathbf{x})\Phi_u \end{bmatrix} \tau_n(k\Delta t)\, d\Gamma,$$

$$\sum_{k=0}^{N} \ddot{\boldsymbol{\lambda}}_k^T \frac{\partial \mathbf{F}_k^{\text{elem}}}{\partial \xi_{mn}} = \sum_{k=0}^{N} \ddot{\boldsymbol{\lambda}}_{k,\text{load}}^T \int_{\Gamma_{\text{load}}} \begin{bmatrix} \theta_{m1}(\mathbf{x})\Phi_u \\ \theta_{m2}(\mathbf{x})\Phi_u \end{bmatrix} \tau_n(k\Delta t)\, d\Gamma, \tag{A2}$$

where, $\ddot{\boldsymbol{\lambda}}_{k,\text{load}}$ contains the values of adjoint variable corresponding to the degrees-of-freedom represented by rows of vector Φ_u on Γ_{load}.

A2 Source location optimization

For any given load location parameter η_m, the derivative of $\mathcal{A}$ is given by,

$$\mathcal{A}_{\eta_m}(\boldsymbol{u},\, \boldsymbol{p},\, \boldsymbol{f}) = \sum_{i=0}^{N} \ddot{\boldsymbol{\lambda}}_i^T \frac{\partial \mathbf{F}_i}{\partial \eta_m}. \tag{A3}$$

For each element,

$$\mathbf{F}_k^{\text{elem}} = \sum_{i=1}^{n_s} \int_{\Gamma_{\text{load}}} \begin{bmatrix} \theta_{i1}(\mathbf{x}, \eta_i)\Phi_u \\ \theta_{i2}(\mathbf{x}, \eta_i)\Phi_u \end{bmatrix} \sum_{j=1}^{n_f} \xi_{ij}\tau_j(k\Delta t)\, d\Gamma,$$

$$\frac{\partial \mathbf{F}_k^{\text{elem}}}{\partial \eta_m} = \int_{\Gamma_{\text{load}}} \begin{bmatrix} \frac{\partial \theta_{m1}(\mathbf{x},\eta_m)}{\partial \eta_m} \Phi_u \\ \frac{\partial \theta_{m2}(\mathbf{x},\eta_m)}{\partial \eta_m} \Phi_u \end{bmatrix} \sum_{j=1}^{n_f} \xi_{mj} \tau_j(k\Delta t)\, d\Gamma,$$

$$\sum_{k=0}^{N} \ddot{\boldsymbol{\lambda}}_{\text{k}}^T \frac{\partial \mathbf{F}_k^{\text{elem}}}{\partial \eta_m} = \sum_{k=0}^{N} \ddot{\boldsymbol{\lambda}}_{k,\text{load}}^T \int_{\Gamma_{\text{load}}} \begin{bmatrix} \frac{\partial \theta_{m1}(\mathbf{x},\eta_m)}{\partial \eta_m} \Phi_u \\ \frac{\partial \theta_{m2}(\mathbf{x},\eta_m)}{\partial \eta_m} \Phi_u \end{bmatrix} \cdot \sum_{j=1}^{n_f} \xi_{mj} \tau_j(k\Delta t)\, d\Gamma, \tag{A4}$$

where, $\ddot{\boldsymbol{\lambda}}_{k,\text{load}}$ contains the values of adjoint variable corresponding to the degrees-of-freedom represented by rows of vector Φ_u on Γ_{load}.

APPENDIX B: ELEMENT MATRICES

Here, we present concise definitions of element matrices that form the global matrices in eq. (12). A detailed description, and definitions of parameters α_i $(i = 1, 2)$, β_i $(i = 1, 2)$ etc., can be found in Kucukcoban & Kallivokas (2013). We define the following symbols to simplify the equations:

$$D_1 = K_{\text{a}} - \frac{2}{3} G_{\text{a}} + \alpha^2 \frac{R}{\phi^2},\ D_2 = \frac{R}{\phi^2},\ D_3 = \frac{1 + C_1}{\phi},\ D_4 = \frac{1}{\kappa} = \frac{\eta}{k},\ D_5 = K_{\text{b}} - \frac{2}{3} G_{\text{b}}. \tag{B1}$$

$$D\mathbf{M}_{pq}^{\text{loc}} = \int_{\Omega_{\text{loc}}} D \Phi_p \Phi_q^T d\Omega, \quad D\mathbf{Q}_{ij,pq}^{\text{loc}} = \int_{\Omega_{\text{loc}}} D \frac{\partial \Phi_p}{\partial x_i} \frac{\partial \Phi_q^T}{\partial x_j} d\Omega, \tag{B2}$$

$$\mathbf{A}_{ijk} = \int_{\Omega_{\text{PML}}} i_j \frac{\partial \Phi_u}{\partial x_k} \Psi^T d\Omega, \quad \mathbf{F}^i = \int_{\Gamma_{\text{load}}} \Phi_u \mathbf{f}^i d\Gamma, \tag{B3}$$

$$\begin{aligned} \mathbf{N}_{ik} &= \int_{\Omega_{\text{PML}}} k \frac{2G + D_5}{4G(G + D_5)} \Psi \Psi^T d\Omega, \quad \text{if } i = 1, \\ &= \int_{\Omega_{\text{PML}}} k \frac{D_5}{4G(G + D_5)} \Psi \Psi^T d\Omega, \quad \text{if } i = 2, \\ &= \int_{\Omega_{\text{PML}}} k \frac{1}{G} \Psi \Psi^T d\Omega, \quad \text{if } i = 3. \end{aligned} \tag{B4}$$

Element matrices for the poroelastic inclusion:

$$\mathbf{M}_{\text{a}} = \begin{bmatrix} \rho_f D_3 \mathbf{M}_{ww}^{\text{a}} & 0 & \rho_f \mathbf{M}_{wu}^{\text{a}} & 0 \\ 0 & \rho_f D_3 \mathbf{M}_{ww}^{\text{a}} & 0 & \rho_f \mathbf{M}_{wu}^{\text{a}} \\ \rho_f \mathbf{M}_{uw}^{\text{a}} & 0 & \rho_{\text{a}} \mathbf{M}_{uu}^{\text{a}} & 0 \\ 0 & \rho_f \mathbf{M}_{uw}^{\text{a}} & 0 & \rho_{\text{a}} \mathbf{M}_{uu}^{\text{a}} \end{bmatrix}, \tag{B5}$$

$$\mathbf{C}_{\text{a}} = \begin{bmatrix} D_4 \mathbf{M}_{ww}^{\text{a}} & 0 & 0 & 0 \\ 0 & D_4 \mathbf{M}_{ww}^{\text{a}} & 0 & 0 \\ 0 & 0 & 0 & 0 \\ 0 & 0 & 0 & 0 \end{bmatrix}, \tag{B6}$$

$$\mathbf{K}_{\text{a}} = \begin{bmatrix} D_2 \mathbf{Q}_{11,ww}^{\text{a}} & D_2 \mathbf{Q}_{12,ww}^{\text{a}} & \alpha D_2 \mathbf{Q}_{11,wu}^{\text{a}} & \alpha D_2 \mathbf{Q}_{12,wu}^{\text{a}} \\ D_2 \mathbf{Q}_{21,ww}^{\text{a}} & D_2 \mathbf{Q}_{22,ww}^{\text{a}} & \alpha D_2 \mathbf{Q}_{21,wu}^{\text{a}} & \alpha D_2 \mathbf{Q}_{22,wu}^{\text{a}} \\ \alpha D_2 \mathbf{Q}_{11,uw}^{\text{a}} & \alpha D_2 \mathbf{Q}_{12,uw}^{\text{a}} & (2G + D_1) \mathbf{Q}_{11,uu}^{\text{a}} + G \mathbf{Q}_{22,uu}^{\text{a}} & G \mathbf{Q}_{21,uu}^{\text{a}} + D_1 \mathbf{Q}_{12,uu}^{\text{a}} \\ \alpha D_2 \mathbf{Q}_{21,uw}^{\text{a}} & \alpha D_2 \mathbf{Q}_{22,uw}^{\text{a}} & G \mathbf{Q}_{12,uu}^{\text{a}} + D_1 \mathbf{Q}_{21,uu}^{\text{a}} & (2G + D_1) \mathbf{Q}_{22,uu}^{\text{a}} + G \mathbf{Q}_{11,uu}^{\text{a}} \end{bmatrix}. \tag{B7}$$

Element matrices for the elastic domain:

$$\mathbf{M}_{\text{reg}} = \begin{bmatrix} \rho_b \mathbf{M}_{uu}^{\text{reg}} & 0 \\ 0 & \rho_b \mathbf{M}_{uu}^{\text{reg}} \end{bmatrix}, \quad \mathbf{C}_{\text{reg}} = \begin{bmatrix} 0 & 0 \\ 0 & 0 \end{bmatrix}, \tag{B8}$$

$$\mathbf{K}_{\text{reg}} = \begin{bmatrix} (2G + D_5)\,\mathbf{Q}^{\text{reg}}_{11,uu} + G\mathbf{Q}^{\text{reg}}_{22,uu} & G\mathbf{Q}^{\text{reg}}_{21,uu} + D_5\mathbf{Q}^{\text{reg}}_{12,uu} \\ G\mathbf{Q}^{\text{reg}}_{12,uu} + D_5\mathbf{Q}^{\text{reg}}_{21,uu} & (2G + D_5)\,\mathbf{Q}^{\text{reg}}_{22,uu} + G\mathbf{Q}^{\text{reg}}_{11,uu} \end{bmatrix}. \tag{B9}$$

Element matrices for the PMLs:

$$\mathbf{M}_{\text{PML}} = \begin{bmatrix} \rho_b \mathsf{a}\mathbf{M}^{\text{PML}}_{uu} & 0 & 0 & 0 & 0 \\ 0 & \rho_b \mathsf{a}\mathbf{M}^{\text{PML}}_{uu} & 0 & 0 & 0 \\ 0 & 0 & -\mathbf{N}_{1\mathsf{a}} & \mathbf{N}_{2\mathsf{a}} & 0 \\ 0 & 0 & \mathbf{N}_{2\mathsf{a}} & -\mathbf{N}_{1\mathsf{a}} & 0 \\ 0 & 0 & 0 & 0 & -\mathbf{N}_{3\mathsf{a}} \end{bmatrix}, \tag{B10}$$

$$\mathbf{C}_{\text{PML}} = \begin{bmatrix} \rho_b \mathsf{b}\mathbf{M}^{\text{PML}}_{uu} & 0 & \mathbf{A}_{\alpha 21} & 0 & \mathbf{A}_{\alpha 12} \\ 0 & \rho_b \mathsf{b}\mathbf{M}^{\text{PML}}_{uu} & 0 & \mathbf{A}_{\alpha 12} & \mathbf{A}_{\alpha 21} \\ \mathbf{A}_{\alpha 21} & 0 & -\mathbf{N}_{1\mathsf{b}} & \mathbf{N}_{2\mathsf{b}} & 0 \\ 0 & \mathbf{A}_{\alpha 12} & \mathbf{N}_{2\mathsf{b}} & -\mathbf{N}_{1\mathsf{b}} & 0 \\ \mathbf{A}_{\alpha 12} & \mathbf{A}_{\alpha 21} & 0 & 0 & -\mathbf{N}_{3\mathsf{b}} \end{bmatrix}, \tag{B11}$$

$$\mathbf{K}_{\text{PML}} = \begin{bmatrix} \rho_b \mathsf{c}\mathbf{M}^{\text{PML}}_{uu} & 0 & \mathbf{A}_{\beta 21} & 0 & \mathbf{A}_{\beta 12} \\ 0 & \rho_b \mathsf{c}\mathbf{M}^{\text{PML}}_{uu} & 0 & \mathbf{A}_{\beta 12} & \mathbf{A}_{\beta 21} \\ \mathbf{A}_{\beta 21} & 0 & -\mathbf{N}_{1\mathsf{c}} & \mathbf{N}_{2\mathsf{c}} & 0 \\ 0 & \mathbf{A}_{\beta 12} & \mathbf{N}_{2\mathsf{c}} & -\mathbf{N}_{1\mathsf{c}} & 0 \\ \mathbf{A}_{\beta 12} & \mathbf{A}_{\beta 21} & 0 & 0 & -\mathbf{N}_{3\mathsf{c}} \end{bmatrix}. \tag{B12}$$